

New Journal of Physics

The open access journal at the forefront of physics

Deutsche Physikalische Gesellschaft 

IOP Institute of Physics

Published in partnership
with: Deutsche Physikalische
Gesellschaft and the Institute
of Physics



PAPER

OPEN ACCESS

RECEIVED
8 March 2021

REVISED
11 May 2021

ACCEPTED FOR PUBLICATION
25 May 2021

PUBLISHED
17 June 2021

Original content from
this work may be used
under the terms of the
[Creative Commons
Attribution 4.0 licence](#).

Any further distribution
of this work must
maintain attribution to
the author(s) and the
title of the work, journal
citation and DOI.



Localized Wannier function based tight-binding models for two-dimensional allotropes of bismuth

Qile Li^{1,2,4} , Jackson S Smith^{2,3,*} , Yuefeng Yin^{1,2,*} , Chutian Wang^{1,2} , Mykhailo V Klymenko³ , Jared H Cole^{2,3,*}  and Nikhil V Medhekar^{1,2,*} 

¹ Department of Materials Science and Engineering, Monash University, Clayton, VIC 3800, Australia

² ARC Centre of Excellence in Future Low-Energy Electronics Technologies, Australia

³ Chemical and Quantum Physics, School of Science, RMIT University, Melbourne, VIC 3001, Australia

⁴ School of Physics and Astronomy, Monash University, Clayton, VIC 3800, Australia

* Authors to whom any correspondence should be addressed.

E-mail: jackson.smith@rmit.edu.au, yuefeng.yin@monash.edu, jared.cole@rmit.edu.au and nikhil.medhekar@monash.edu

Keywords: topological materials, electronic structure, tight-binding model, first-principles calculations

Abstract

With its monoelemental composition, various crystalline forms and an inherently strong spin–orbit coupling, bismuth has been regarded as an ideal prototype material to expand our understanding of topological electronic structures. In particular, two-dimensional bismuth thin films have attracted a growing interest due to potential applications in topological transistors and spintronics. This calls for an effective physical model to give an accurate interpretation of the novel topological phenomena shown by two-dimensional bismuth. However, the conventional semi-empirical approach of adapting bulk bismuth hoppings fails to capture the topological features of two-dimensional bismuth allotropes because the electronic band topology is heavily influenced by crystalline symmetries. Here we provide a new parameterization using localized Wannier functions derived from the Bloch states in first-principles calculations. We construct new tight-binding models for three types of two-dimensional bismuth allotropes: a Bi (111) bilayer, bismuthene and a Bi (110) bilayer. We demonstrate that our tight-binding models can successfully reproduce the electronic and topological features of these two-dimensional allotropes. Moreover, these tight-binding models can be used to explain the physical origin of the occurrence of novel band topology and the perturbation effects in these bismuth allotropes. In addition, these models can serve as a starting point for investigating the electron/spin transport and electromagnetic response in low-dimensional topological devices.

1. Introduction

The discovery of spin–orbit coupling (SOC) induced topological phase transitions in electronic structure have led to a rapidly growing interest in the topological electronics and spintronics applications [1, 2]. Due to an intrinsically strong SOC, bismuth and its compounds offer a rich playground for the development and application of topological band theories [3]. The electronic structure and band topology of pure bismuth depends considerably on its crystal structure. Bulk bismuth is a semimetal which has previously been considered to be topologically trivial [4], but recent reports have suggested nontrivial band topology and exotic, higher-order topological features such as hinge states [5, 6]. When the bismuth lattice is confined to two dimensions, the resulting bismuth allotropes have been predicted to offer many topologically nontrivial and distinct phases [7]. For instance, the Bi (111) bilayer—a layer of bismuth atoms arranged in a buckled configuration—is predicted to have a quantum spin Hall (QSH) phase [8]. On the other hand, bismuthene—a graphene-like planar layer of bismuth arranged in a honeycomb lattice—is reported to be a topological crystalline insulator (TCI) [9, 10]. Due to the diversity of nontrivial topological phases,

two-dimensional bismuth allotropes have attracted extensive interest in recent years as a potential candidate for building novel topological electronic and spintronic devices [5, 11, 12].

Recent experiments have demonstrated that manipulating the band topology of different 2D bismuth allotropes can lead to many exotic physical phenomena. For example, it has been shown that the ultrathin Bi (111) films can be used to tune topological edge states when interfaced with other 2D materials [13–15]. In a Bi (110) bilayer, elastic strains and external electric fields can significantly affect the stability of its topological phase due to its sensitivity to atomic buckling and charge doping [16, 17]. For planar bismuthene, recent experiments and calculations have demonstrated a controllable orbital-filtering QSH effect due to selective bonding with a silicon carbide substrate [11]. Despite the recent progress, a unified understanding of the correlation between the crystalline symmetries of 2D bismuth allotropes and their topological phases is still being developed.

Previous attempts to understand the influence of the crystal symmetries of 2D bismuth on electronic structure have largely been limited to semi-empirical tight-binding (TB) models of the bulk bismuth [4, 18, 19]. However, as we illustrate later, these models cannot be used for 2D allotropes of bismuth for several reasons. First, the symmetry of two-dimensional bismuth is different from that of the bulk—the semi-empirical TB model cannot faithfully reflect the symmetry reduction from bulk to a surface-like structure. Moreover, the semi-empirical model does not consider the relaxation of atomic positions in the two-dimensional layer relative to the bulk. A notable example is the planar honeycomb structure of bismuthene, which cannot be directly related to the bulk bismuth symmetry. Consequently, these issues lead to poor agreement between the band structure computed from the semi-empirical model and first-principles density functional theory (DFT) [20].

To gain physical insights into correlation between crystal symmetry and topological phases of 2D allotropes of bismuth, here we develop effective TB models of Bi (111) and Bi (110) bilayers as well as bismuthene using localized Wannier functions constructed from first-principles calculations [21]. Wannier functions offer a natural choice of an orthonormal basis set due to the connection between the charge center of these functions and the Berry phase of Bloch states [22]. These functions can be exponentially localized to either atom centers or interstitial sites, and are therefore similar to the atomic orbitals. Furthermore, the Wannier basis set can be constructed without the need to fit free parameters to the band structures obtained from DFT or experiments. Wannier functions thereby allow us to construct a model Hamiltonian for each allotrope with relatively few parameters and yet still provide an accurate description of their band structure and its relationship with the crystal symmetry. These Wannier function based Hamiltonians can be further employed to investigate charge and spin carrier transport in electronic devices based on low-dimensional topological materials.

This article is organized as follows. In section 2 we discuss the limitations in the applicability of the semi-empirical TB parameters from bulk bismuth to a Bi (111) bilayer. We then introduce a method for parameterizing new TB models from the first-principles calculations in section 3. First we outline our density-functional methods in section 3.1, then in section 3.2 we explain the construction of the TB models from localized Wannier functions, including constraints due to the symmetries of the crystallographic lattices. Finally, in section 4 we discuss the results of our TB model for a Bi (111) bilayer (section 4.1), bismuthene (section 4.2), and a Bi (110) bilayer (section 4.3). We discuss both the key steps of model construction and the implications of our models on the electronic and topological properties of two-dimensional bismuth allotropes. We conclude in section 5.

2. The applicability of tight binding parameters from bulk to a bilayer

The electronic properties of Bi (111) bilayers [8, 20] are typically modeled using semi-empirical TB parameters derived for bulk bismuth [4]. For example, this strategy was adopted in [8, 20], by using the hopping parameters of bulk bismuth to model a bismuth bilayer, with the SOC strength (λ) increased from its bulk value to better fit the energy splittings between the bands of a bilayer when compared to DFT calculations. In the following we will investigate the validity of this approach, as outlined in [8, 20], and determine if applying bulk TB parameters to a two dimensional structure can faithfully reproduce all critical electronic features of the topologically nontrivial Bi (111) bilayer.

We use TB parameters for bulk bismuth to calculate the band structure of a Bi (111) bilayer but truncate these parameters by retaining only the hoppings inside the bilayer [8]. All calculations were performed using NanoNET, an extendable Python framework for electronic structure computations based on the TB method [23]. The resulting band structure is shown in the colored lines of figure 1. The SOC strength is taken from the bulk value (1.5 eV). In this figure we have also plotted a band structure for the bilayer computed from DFT (black lines) for reference (see section 3.1 for method). There is good agreement between the valence bands (VBs) of TB and DFT for an SOC strength of 1.5 eV but the agreement between

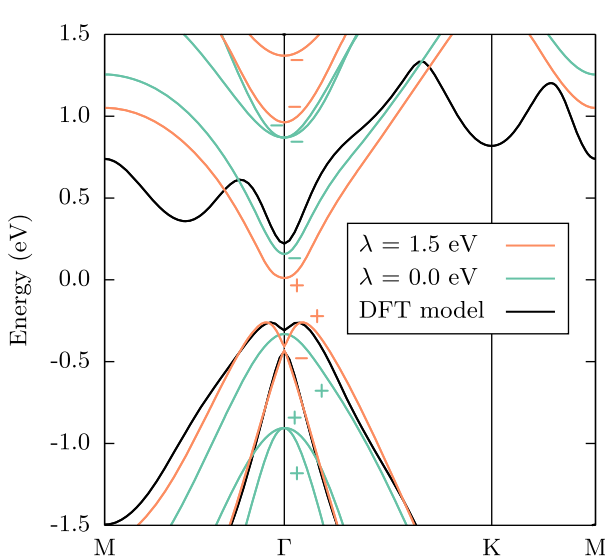


Figure 1. Band structures of a Bi (111) bilayer computed from TB parameters of bulk bismuth [4] with (orange lines) and without (green lines) SOC. The parity of each eigenstate at the Γ point is labeled as either even (+) or odd (-). The band structure predicted by DFT (black lines) has been lowered by 0.25 eV to align the valence bands of the two models.

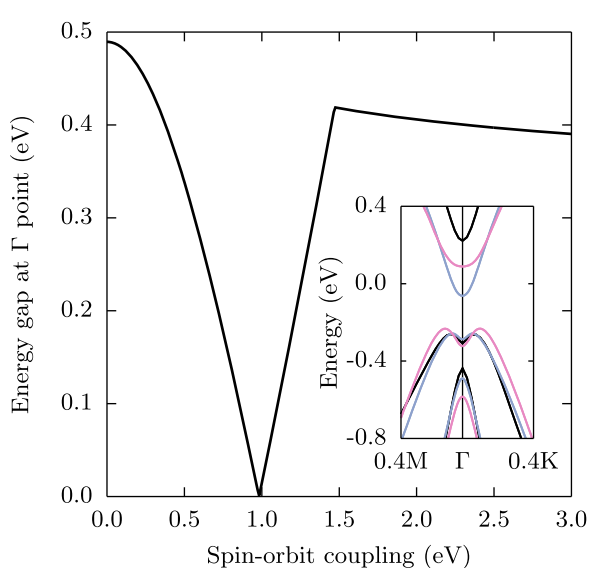


Figure 2. Energy gap between the valence and conduction bands at the Γ point computed from TB parameters of bulk bismuth [4] as a function of SOC. The inset shows band structures of a Bi (111) bilayer computed from the same parameters with SOCs of 1.25 eV (blue lines) and 1.75 eV (pink lines). The band structure of DFT is also shown in the inset (black lines).

the conduction bands (CBs) is poor. The lowest conduction band of the TB model has energy minima at points Γ and M whereas DFT predicts two additional minima, one at K and another along the high symmetry segment $M \rightarrow \Gamma$.

Another property of interest is band inversion, i.e. the exchange of a crystal's electronic properties (e.g. parity) between its CBs and VBs. The parity of each eigenstate at the Γ point in figure 1 is labeled as either even (+) or odd (-). The parities of the bands shown in the figure are even for the VBs and odd for the CBs with no SOC ($\lambda = 0.0$ eV). When we use the bulk SOC value of 1.5 eV, the parity of the second highest valence band and lowest conduction band are exchanged. This is in good agreement with a previous study that assumes a Bi (111) film retains the bulk lattice parameter at about 20–50 nm of film thickness [24]. However, several reports have shown that when bismuth films are reduced to only one bilayer thickness, the change of parities occurs between the highest valence band and lowest conduction band, contrary to the data presented in figure 1 [13, 25]. This contrasting behavior has been associated with the change of the lattice parameter from its bulk value [13, 25].

SOC also significantly affects the band gap in a Bi (111) bilayer. Figure 2 shows the variation of the band gap at the Γ point between the highest valence band and the lowest conduction band as a function of the SOC strength. The maximum energy gap that can be achieved at the Γ point by increasing the strength of the SOC is approximately 0.4 eV. This gap is smaller than the gap computed from DFT (see inset of figure 2) which typically underestimates band gaps compared to their experimental values [26]. We have found that the band splitting agrees better with the DFT results if we increase the SOC strength in the TB model to 1.8 eV, as suggested by [20]. However, the band shape and the exchange of parities still do not agree with *ab initio* calculations and experimental observations [25, 27]. Based on the results above, we conclude that an effective TB model of two-dimensional bismuth layered materials cannot be achieved by using bulk hopping parameters, even by tuning the strength of SOC. Consequently, a new model is needed for 2D allotropes of bismuth that adapts to the structural changes of the material when reduced from the bulk to a thin film.

3. Tight binding models from Wannier functions

3.1. Density-functional method

We first obtained the electronic structure of the 2D allotropes of bismuth through DFT as implemented in the Vienna *Ab Initio* Simulation Package [28, 29]. Exchange and correlation effects were captured by the generalized gradient approximation and the Perdew–Burke–Ernzerhoff functional [30]. The atomic structures of the allotropes were first optimized prior to a self-consistent convergence of the electronic structure using a Γ -centered $21 \times 21 \times 1$ k -point grid. The energy cutoff for the plane-wave basis used was 600 eV. Wavefunctions obtained using DFT were utilized to construct TB models based on Wannier functions using the code Wannier90 [31], as discussed in the next section.

3.2. Construction of Wannier tight binding models and symmetry constraints

For periodic systems with translational symmetry, the one-particle states can be expressed by the Bloch state $|\psi_{nk}\rangle$ with band index n and crystal momentum \mathbf{k} . When deriving parameters for the hopping of an electron from one orbital in a crystal to another it is more convenient to consider localized orbitals rather than Bloch states because the latter are delocalized. Wannier functions are one such choice of localized orbitals and they can be constructed by the inverse Fourier transform of a Bloch state. In this way we can obtain a real-space Wannier TB Hamiltonian by a discrete Fourier transformation [32]:

$$\langle \mathbf{0} | \hat{H} | \mathbf{R} \rangle = \frac{1}{N} \sum_{\mathbf{q}} e^{-i\mathbf{q} \cdot \mathbf{R}} U_{\mathbf{q}}^{\dagger} E_{\mathbf{q}} U_{\mathbf{q}}, \quad (1)$$

where \mathbf{R} is a real-space lattice vector, $\mathbf{0}$ is the real-space lattice vector that defines the home cell [i.e. $\mathbf{R} = (0, 0, 0)$], N is the number of points in the k -point grid and $E_{\mathbf{q}}$ are eigenvalues from DFT. $U_{\mathbf{q}}$ is a unitary transformation that takes the Bloch state at point \mathbf{q} in k -space to a rotated Bloch state in the Wannier gauge [32], i.e.

$$|\tilde{\psi}_{nk}\rangle = \sum_m U_{mn}^{(\mathbf{k})} |\psi_{mk}\rangle, \quad (2)$$

where n and m are band indices. The corresponding reciprocal space TB Hamiltonian $H_{\alpha\beta}(\mathbf{k})$ can then be expressed as a Fourier transformation from the real-space Hamiltonian $H_{\alpha\beta}(\mathbf{R})$ to k -space:

$$H_{\alpha\beta}(\mathbf{k}) = \sum_{\mathbf{R}} e^{i\mathbf{k} \cdot (\mathbf{R} + \tau_{\beta} - \tau_{\alpha})} H_{\alpha\beta}(\mathbf{R}), \quad (3)$$

where the subscript $\alpha\beta$ denotes a Hamiltonian matrix element that corresponds to hopping from orbital α at τ_{α} in the home cell to orbital β at τ_{β} within a cell at \mathbf{R} . $H_{\alpha\beta}(\mathbf{R})$ can be further expanded as:

$$H_{\alpha\beta}(\mathbf{R}) = t_{\alpha\beta}(\mathbf{R} - \mathbf{0}) = \langle \mathbf{0} + \tau_{\alpha} | H | \mathbf{R} + \tau_{\beta} \rangle, \quad (4)$$

where $t_{\alpha\beta}(\mathbf{R} - \mathbf{0})$ represents the hopping parameter between neighboring atomic orbitals α in the home cell and β in the cell \mathbf{R} extracted from the Wannier TB Hamiltonian. For simplicity, we have used a simple numerical subscript t_n in later presentation of our TB models. A detailed discussion of the extraction process and the role of each hopping parameter can be found in the appendix A.

Next we discuss the symmetry constraints on this Hamiltonian. The representations generated from the method implemented in Wannier90 [33] often contain small numerical errors that can break the symmetries of the crystal's energy bands. We correct these errors and restore the corresponding constraints

on the crystal's symmetry. Our Hamiltonians satisfy the following symmetry constraints in k -space and real-space respectively [33]:

$$H(\mathbf{k}) = D(g)H(g^{-1}\mathbf{k})D^{-1}(g) \quad g \in G \quad (5)$$

$$H_{ij}(\mathbf{R}') = \sum_{\alpha,\beta} D_{i\alpha}(g)H_{\alpha\beta}(\mathbf{R})D_{\beta j}^{-1}(g) \quad g \in G. \quad (6)$$

$D(g)$ is the matrix representation of the symmetry operation g , which is an element of symmetry group G . The matrix representations used for the 2D allotropes of bismuth (D_{3d} for the Bi (111) bilayer, D_{6h} for bismuthene and D_{2h} for the Bi (110) bilayer) are given in appendix A. The subscripts α and β are the orbital indices before the symmetry operation and i and j are the corresponding indices after this operation. \mathbf{R}' is a lattice vector that defines the cell's position after the symmetry operation.

To ensure our Hamiltonian matrix satisfies each symmetry constraint for a particular allotrope, we take a group average over all Hamiltonians transformed by the symmetry operations in G through equation (6). This yields a symmetrized Hamiltonian [33]:

$$\tilde{H}_{\alpha\beta}(\mathbf{R}) = \frac{1}{l} \sum_G D_{i\alpha}^{-1}(g)H_{ij}(\mathbf{R}')D_{\beta j}(g), \quad (7)$$

where l is the number of elements in the symmetry group.

4. Results

To constrain our basis functions to crystal symmetries and fix Wannier orbitals to atomic positions, we construct our TB Hamiltonian from a spinless case without performing maximal localization on Wannier functions. We have also treated SOC independently, evaluating it in the basis of atomic orbitals and then fitting the SOC parameters by comparing to the bands of DFT. In the construction process we emphasize the necessity of determining the symmetry properties of electronic bands in constructing the TB model for each allotrope. The SOC effects are also treated differently for each bismuth allotrope considering the changes in crystalline symmetries.

In the following subsections we present the symmetry of the crystal structures, properties of the basis functions and construction of the TB models for each allotrope. We address the effectiveness of our symmetrized models in describing the electronic structure of two-dimensional bismuth allotropes compared to the semi-empirical approach, and briefly discuss how the model can be used to explain the nontrivial band topology occurring in bismuth allotropes. It should be noted that here we highlight for brevity the key steps in constructing the TB model and focus on how these models can reflect the electronic and topological properties of each bismuth allotrope. The details of the process of deriving individual TB hopping parameters, the intrinsic SOC hoppings, and the basis function of the irreducible representations (IRs) are provided in appendix A.

4.1. Bi (111) bilayer

The Bi (111) bilayer has a quasi-2D honeycomb structure characterized by an in-plane lattice constant of 4.33 Å and an out-of-plane buckling with an intra-layer spacing of approximately 1.74 Å. These optimized lattice constants are consistent with previous literature [34]. There are two inequivalent atoms in the primitive cell as shown in figure 3. The crystal structure of the Bi (111) bilayer has a symmorphic space group symmetry of $P\bar{3}m1$ (D_{3d}^3 , SG164). The symmetry generators for its point subgroup include the identity (E), inversion (P), threefold rotation along the z direction (C_{3z}), and three twofold rotations (C_2). From the orbital characters obtained from our DFT calculations, we find the s orbitals form an isolated set of bands well below the Fermi level. Closer to the Fermi level, p orbitals form two sets of isolated bands: three VBs and three CBs, as shown in figure 4. We therefore choose to include only p orbitals in our TB model to describe bands near the Fermi level.

We first consider the spinless TB model. The number of nearest-neighbor (NN) hoppings to include is a critical parameter when we construct the model. To investigate the relationship between neighbor interactions and the agreement of our model with DFT, we calculate the average energy difference between the two models along a path of high symmetry in the first Brillouin zone (FBZ). We find that a Hamiltonian with second NN interactions can well reproduce the topological properties of the Bi (111) bilayer, with good agreement to the occupied states. However, the inclusion of up to fourth NNs is needed to recover the features of unoccupied bands (see figure 4(b)), but at the cost of requiring more hopping parameters. The details of deriving the spinless TB model for Bi (111) bilayer are given in appendix A where the hopping parameters and the procedure to generate the Hamiltonian using symmetry properties are listed.

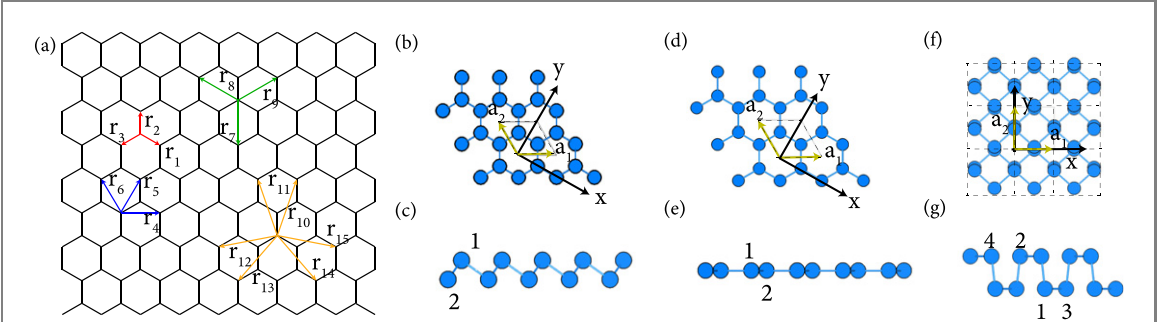


Figure 3. (a) Top-down view of first-nearest neighbor (red arrows), second-nearest neighbor (blue arrows), third-nearest neighbor (green arrows), and fourth-nearest neighbors (orange arrows) hopping vectors of bismuth allotropes. (b)–(g) Schematics of the two-dimensional allotropes of bismuth, with atoms (blue spheres) and primitive cells (solid black lines). (b) Top down view and (c) side view of a Bi (111) bilayer. (d) Top down view and (e) side view of bismuthene. (f) Top down view and (g) side of a Bi (110) bilayer. The unit cells of these bismuth allotropes are shown in (b), (d) and (f) in dashed lines. In subfigures (c), (e) and (g), each atom in the primitive cell is labeled with an index ranging from 1 to 4. The labels a_1 , a_2 and x , y denote the lattice vector and Cartesian axis respectively. The precise coordinates of unit cell lattice vectors, atomic coordinates and hopping vectors are given in appendix A.

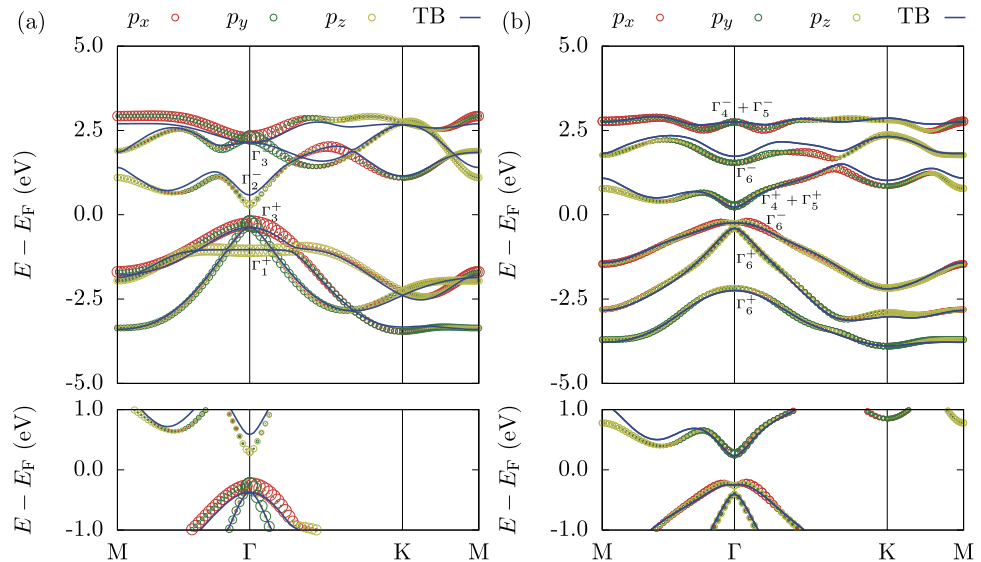


Figure 4. Bilayer bismuth (111) band structure (a) without and (b) with SOC by including neighboring interactions up to fourth NNs. Energy bands from our TB model are shown as solid dark blue lines. Energy bands from DFT are plotted as circles, with p_z in yellow, p_x in red and p_y in green. The weights of orbitals are represented by the size of the circles. The band structure is plotted in the range of $(E_F - 5 \text{ eV}, E_F + 5 \text{ eV})$ with the zoom-in figure of band structure $\pm 1 \text{ eV}$ around the Fermi level shown below.

Next, we add SOC interactions to the spinless Hamiltonian. Conventionally, the SOC contribution to the spinor Hamiltonian is expressed as a function of the on-site SOC strength, λ :

$$H_{\text{soc}} = \lambda \hat{\mathbf{L}} \cdot \hat{\mathbf{S}}. \quad (8)$$

The on-site SOC strength λ has a large effect on inducing band inversion at the Γ point. At $\lambda = 1.1 \text{ eV}$, the system experiences a gap-closing phase transition, with exchange of parity character between occupied and unoccupied states. The VB and CB near the Fermi level will be separated further apart if λ is further increased. We notice a particular feature in the DFT bands, which shows a small segment of nonzero curvature in the highest VB near Γ just below the Fermi level (figure 4(b)). We can obtain this feature with large λ at the expense of band mismatches in other parts of the occupied bands. This issue can be resolved when we introduce a next-nearest neighbor SOC term, which reflects the strong SOC strength of bismuth and the threefold rotation symmetry of the honeycomb lattice. The form of this term is expressed as [35]:

$$H_{\text{I}} = i \sum_{\{m,n\}} \sum_{\{\alpha,\alpha\}} \lambda_{mn} [\sigma_z]_{\alpha\alpha} c_{m,\alpha}^\dagger c_{n,\alpha} + \text{h.c.}, \quad (9)$$

Table 1. Inversion eigenvalues of the occupied states at TRIM for the Bi (111) bilayer. The sign in the bracket denotes parity for spinless states. The occupied states are numbered from low energy to high energy and we have used the same indices for degenerate bands.

TRIM\occupied states	1	2	3
(0,0,0)	+(+)	+(+)	-(-)
($\frac{1}{2}$,0,0)	+(+)	-(-)	-(-)
(0, $\frac{1}{2}$,0)	+(+)	-(-)	-(-)
($\frac{1}{2}$, $\frac{1}{2}$,0)	+(+)	-(-)	-(-)

where H_I is the intrinsic SOC originating from the buckling of the (111) bilayer, λ_{mn} is the effective SOC strength associated with hopping from orbital m in home cell to orbital n in next-nearest neighbor cell, and $[\hat{\sigma}_z]_{\alpha\alpha}$ is the element (α, α) of the Pauli matrix. As discussed by Kochan *et al* [35], only diagonal elements in the spin basis are non-zero for intrinsic SOC. Combining symmetry considerations and the requirement of Hermiticity, we obtain the intrinsic next-nearest SOC term λ_{mn} in the form of a 3×3 matrix with 6 independent parameters (more detailed derivation of this term is given in appendix A):

$$\lambda_{mn} = \begin{pmatrix} \lambda_1 & \lambda_2 & \lambda_3 \\ \lambda_2 & \lambda_4 & \lambda_5 \\ -\lambda_3 & -\lambda_5 & \lambda_6 \end{pmatrix}. \quad (10)$$

We obtain the parameters λ_1 to λ_6 from first-principles again and the on-site SOC term λ is tuned to fit the energy bands at Γ near the Fermi level. We have listed the values of these SOC parameters together with other hopping parameters in table 4.

This concludes the construction process of our spinless and spinor TB models. An advantage of these models is that they use minimal parameters to accurately reproduce the electronic and topological structure of the bismuth allotropes studied here. We now examine the band structure of Bi (111) bilayer with the aid of band representations. Figure 4 shows the IRs at Γ obtained from our TB models and corresponding orbital characters from DFT calculations shown in circles. Table 5 summarizes the basis functions of IRs. The notation we use for IRs is consistent with Koster's [36].

In the spinless case (figure 4(a)), the highest VB (with IR Γ_3^+ and basis functions of $\{|p_x^+\rangle, |p_y^+\rangle\}$) has a double degeneracy protected by the threefold rotation symmetry of the crystal structure and the lowest CB belongs to the Γ_2^- IR, which consists of an equal mixing of p_z orbitals from the two atoms in the primitive cell. After taking electron spins into account, the new double group IRs near the Fermi level are: $\Gamma_3^+ \otimes \Gamma_4^+ = \Gamma_4^+ \oplus \Gamma_5^+ \oplus \Gamma_6^+$ and $\Gamma_2^- \otimes \Gamma_6^+ = \Gamma_6^-$. In other words, the product of the basis functions for the highest VB (corresponding to Γ_3^+) with spinor basis functions can be decomposed into a direct sum of states Γ_4^+, Γ_5^+ and Γ_6^+ , and a product of the lowest CB Γ_2^- state with a spinor yields an anti-symmetric Γ_6^- state. As a result of both TR and inversion symmetry, all the eigenstates are doubly degenerate. In addition, one dimensional IRs Γ_4^\pm and Γ_5^\pm are related by TR symmetry and form a Kramer pair.

The band inversion is characterized by the exchange of states between $\Gamma_4^+ \oplus \Gamma_5^+$ and Γ_6^- . The accompanying exchanging of parity between occupied and unoccupied states gives rise to the topological nontriviality of the system. The \mathbb{Z}_2 topological invariant can be calculated simply by taking parity values at four time reversal invariant momenta (TRIM) points in the FBZ [37]. Inversion parity eigenvalues of occupied states at TRIM are listed in table 1. The \mathbb{Z}_2 invariant of 1 calculated from our TB for Bi (111) bilayer is consistent with the values reported in literature using DFT methods [25].

Finally we discuss the connection between our Wannier-based TB model and the structural properties of the Bi (111) bilayer. The electronic structure of Bi (111) bilayer has been known to be sensitive to changes in structural parameters such as in-plane lattice constant and intralayer buckling [38]. In experiments, these structural parameters tend to vary from bulk-like (lattice constant $a = 4.54$ Å) [39, 40] to highly compressive ($a = 4.38$ Å) [13, 41] depending on the choice of the supporting substrate. However, ultrathin Bi (111) films approaching the one atomic layer thickness have been reported to be difficult to grow on substrates, and the low-symmetry Bi (110) layer is preferable to nucleate on the surface due to large lattice mismatch. Currently Bi (111) thin films with less than four atomic layers have only been stabilized in Bi_2Se_3 and Bi_2Te_3 [13, 42]. In these cases, the lattice constant of the thin film is compressed relative to its bulk value ($a = 4.38$ Å). Moreover, a previous theoretical investigation has revealed that the equilibrium lattice constant of a free-standing Bi (111) bilayer is 4.33 Å with a buckling of 1.74 Å.³⁵ These findings are consistent with our relaxed DFT structure, suggesting that our derived TB model can faithfully reflect the structural features of a Bi (111) bilayer.

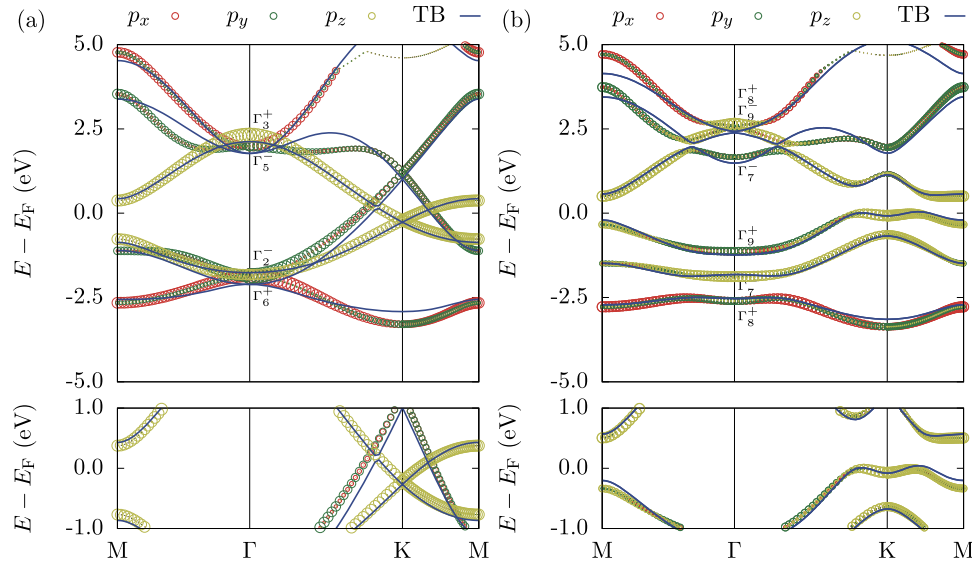


Figure 5. Bismuthene band structure (a) without and (b) with SOC. Energy bands from our TB model are shown as solid dark blue lines. Energy bands from DFT are plotted as circles, with p_z in yellow, p_x in red and p_y in green. The weights of orbitals are represented by the size of the circles. The band structure is plotted in the range of $[E_F - 5 \text{ eV}, E_F + 5 \text{ eV}]$ with the zoom-in figure of band structure $\pm 1 \text{ eV}$ around the Fermi level shown below.

We can further see the importance of these geometrical parameters when we revisit the electronic structure of the semi-empirical model as mentioned in section 2. The lattice constant of the semi-empirical TB model is directly taken from the bulk value ($a = 4.55 \text{ \AA}$ and 1.59 \AA intralayer buckling). When comparing to our TB model using $a = 4.33 \text{ \AA}$ with a buckling of 1.74 \AA , we find that the difference in buckling will significantly affect the bands with large p_z character. We can see changes in the band dispersion along Γ -M for lowest CB and near Γ for highest VB where the p_z states are concentrated. We can also see change of parity order of bands upon including SOC. Further, the more buckled structure leads to larger band gap due to higher intrinsic SOC strength. In conclusion, our TB model provides a reliable picture of the electronic structure of ultrathin Bi (111) films compared to the semi-empirical approach. It should also be noted that it is convenient to incorporate the effect of geometrical changes in Wannier-TB model in future studies.

4.2. Bismuthene

Bismuthene is a 2D allotrope of bismuth arranged in a planar honeycomb crystal structure. Our DFT calculation yields a lattice parameter of 5.35 \AA , which is consistent with a previous theoretical report [34]. The crystal structure has symmetry of space group $P6/mmm$ (D_{6h}^1 , SG191). The symmetry generators for its point group include identity (E), inversion (P), twofold rotations along the z direction (C_{2z}), and two threefold rotations (C_3). By analyzing the orbital character obtained from our DFT calculations, we find that there is negligible hybridization between s and p orbitals. The bands in the vicinity of the Fermi level are mainly contributed by Bi p orbitals (see figure 5). Therefore we choose to include only p orbitals in our TB model of bismuthene to describe the electronic structure near the Fermi level.

For a spinless Hamiltonian, we only need to include hoppings up to second-nearest neighbors to reproduce the electronic band structure, resulting in a TB model with 9 independent hopping parameters after applying the symmetry constraints. Considering spinors, due to the lack of buckling in bismuthene, the SOC interaction can be included by introducing an on-site term where the SOC strength for bismuthene (λ) is taken directly from our *ab initio* calculation as defined in equation (8). The detailed derivation process for the TB model of bismuthene can be found in appendix A. The values of the hopping parameters and the intrinsic SOC strength for bismuthene are presented in table 6.

To understand the band structure better, we have computed the band representations and listed them in table 7 along with the basis functions. Without SOC, the eigenstates formed by spinless p orbitals can be categorized into representations Γ_2^- , Γ_3^+ , Γ_6^+ and Γ_5^- . Γ_3^+ and Γ_6^+ states corresponding to symmetric states formed by out-of-plane p orbitals and in-plane p orbitals respectively. Γ_2^- and Γ_5^- correspond to anti-symmetric states. In the figure 5, it can be seen that the orbital characters from the TB model are consistent with those from DFT calculations.

To analyze the symmetry of the Bloch states with SOC, we introduce spinor representation Γ_7^+ and generate IRs of spinful eigenstates from previous IRs of spinless states by again taking the direct product

Table 2. Inversion eigenvalues of occupied states at TRIM for bismuthene. The sign in the bracket denotes parity for spinless states.

TRIM\occupied states	1	2	3
(0,0,0)	+(+)	-(+)	-(-)
($\frac{1}{2}$,0,0)	-(-)	+(+)	+(+)
(0, $\frac{1}{2}$,0)	-(-)	+(+)	+(+)
($\frac{1}{2}$, $\frac{1}{2}$,0)	-(-)	+(+)	+(+)

with a spinor and decomposing onto IRs of the double group for occupied states: $\Gamma_6^+ \otimes \Gamma_7^+ = \Gamma_9^+ \oplus \Gamma_8^+$, $\Gamma_2^- \otimes \Gamma_7^+ = \Gamma_7^-$. The IRs for states in the CB are obtained in a similar way as Γ_7^- , Γ_8^+ and Γ_9^- . To label the eigenstates, we calculate symmetry eigenvalues at the Γ point and compare with the D_{6h} double group character table listed in tables 12 and 13 in appendix A.

SOC has several effects on the electronic states of bismuthene. First, we notice the degeneracy corresponding to the Γ_6^+ state and Γ_5^- state is lifted. Band exchange happens between the upper two bands in the VB and another two high-energy bands in the CB. Even though SOC exchanges the parity of these two VB states, it does not affect the topological properties of bismuthene because there is no exchange between unoccupied and occupied states. We also see that with SOC the electronic structure of bismuthene undergoes a transition from semimetallic phase to an insulator phase after a band gap opens near the K point.

We confirm this further by calculating the \mathbb{Z}_2 invariant using parity values at TRIM listed in table 2. We have numbered bands from low energy to high energy and neglected spin degeneracy for brevity. The result, that bismuthene has $\mathbb{Z}_2 = 0$, is consistent with previous studies [34].

The free-standing bismuthene has been theoretically proposed as a TCI, with conducting edge states protected by its mirror symmetry [9, 10]. However, the planar bismuthene structure is difficult to stabilize on a substrate in an experimental setting, limiting its usage as a TCI. Recent reports have successfully created a planar bismuthene layer by forming covalent bonding with SiC-(0001) [11]. The covalent interaction induces orbital filtering effect in the band structure of bismuthene and turns bismuthene into a topological insulator [11]. Here we show that we can reproduce this topological phase transition from TCI to TI by adding an on-site energy to p_z hoppings in our TB model. This added potential acts as a perturbation due to the presence of a substrate. Our calculations yield overall band dispersion that is in good agreement with experiments as shown in figure 6. Without SOC (figure 6(a)), it can be clearly see that under such orbital filtering effect, the two p_z bands are shifted away from Fermi level and the bands left mainly consist of p_x and p_y orbitals. A gapless Dirac cone can be seen at the K point. After including SOC (figure 6(b)), a gap of size 1 eV is opened at the K point, close to the reported experimental value of 0.8 eV [11]. We calculate the band representations and found that the representations correspond to basis functions with in-plane p orbitals. A calculation of \mathbb{Z}_2 at four TRIMs yields a nontrivial number 1 with SOC, confirming the phase transition from TCI to TI.

This topological phase transition is directly caused by the shifting of p_z states to the deep occupied states, triggering band inversion and pushing bismuthene from TCI phase into TI phase. The Rashba SOC from the substrate can also be included, but the magnitude of the Rashba effect is relatively weak (about 30 meV), resulting in only a spin splitting of the bands and leaving the band topology unaffected [11]. It is worth pointing out one minor discrepancy in part of the CB, which is possibly due to the difference in the lattice constant used here (5.35 Å) vs 5.27 Å reported for a SiC substrate [11]. Nevertheless, the overall band dispersion is in good agreement with the literature [11]. These results have shown the universality and accuracy of our simplified TB model of planar bismuthene.

4.3. Bi (110) bilayer

A Bi (110) bilayer consists of two layers of planar bismuth. Upon relaxation, we find this 2D allotrope possesses a non-symmorphic crystal symmetry unlike the (110) surface of bulk bismuth, which has been reported experimentally [43]. It is the only bismuth allotrope reported that shows a different non-symmorphic symmetry after relaxation and also topological nontrivial bands. We obtained optimized lattice constants of $a = 4.56$ Å and $b = 4.87$ Å and an intralayer buckling of 3.08 Å after structural relaxation, which is consistent with previous ARPES measurements [43]. The absence of buckling in each planar layer leads to a crystal symmetry of space group $Pmna$ (D_{2h}^7 , SG53). The symmetry generators for this group include two twofold rotations C_{2y} , C_{2z} and two corresponding mirror operations σ_{2y} , σ_{2z} with a glide translation vector of $(\frac{1}{2}, \frac{1}{2}, 0)$. The presence of glide plane symmetry results in additional band degeneracies in the electronic structure. The projected orbital characters from our DFT calculations show that the electronic bands of Bi (110) bilayer near the Fermi level are mainly from p orbitals (see figure 7).

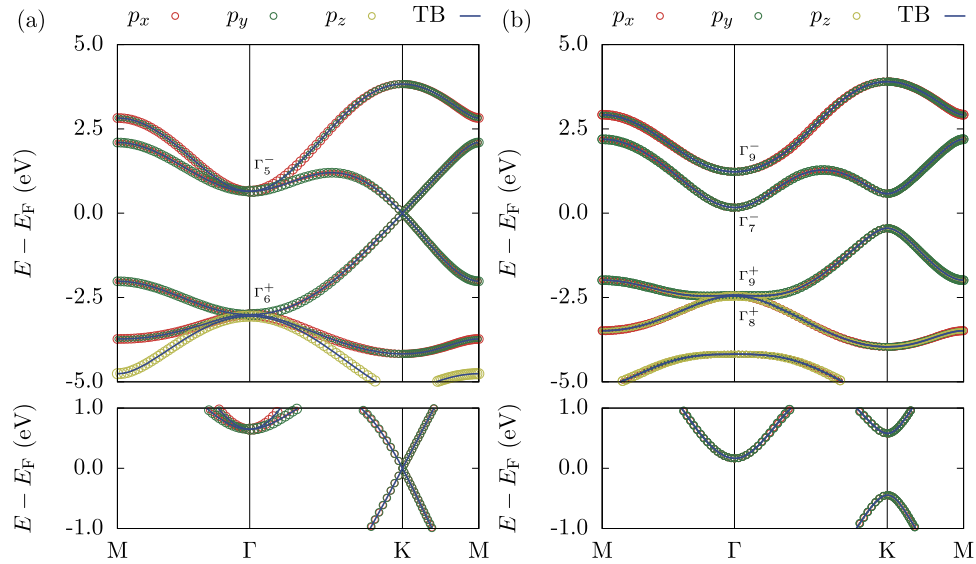


Figure 6. Bismuthene band structure (a) without and (b) with SOC after adding an onsite energy to p_z hoppings. Energy bands from our TB model are shown as solid dark blue lines. The corresponding orbital character calculated from our TB model are plotted as circles, with p_z in yellow, p_x in red and p_y in green. The weights of orbitals are represented by the size of the circles. The band structure is plotted in the range of ($E_F - 5$ eV, $E_F + 5$ eV) with the zoom-in figure of band structure ± 1 eV around the Fermi level shown below.

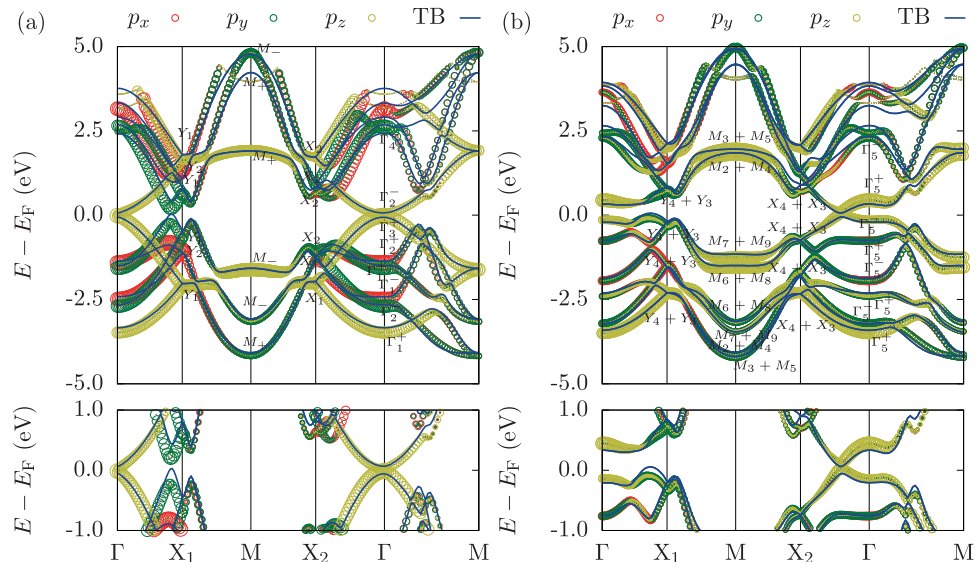


Figure 7. Bi (110) bilayer band structure (a) without and (b) with SOC. Energy bands from our TB model are shown as solid dark blue lines. Energy bands from DFT are plotted as circles, with p_z in yellow, p_x in red and p_y in green. The weights of orbitals are represented by the size of the circles. The band structure is plotted in the range of ($E_F - 5$ eV, $E_F + 5$ eV) with the zoom-in figure of band structure ± 1 eV around the Fermi level shown below.

The contribution of s orbitals is to energy bands far below the Fermi level and in this case isolated from the rest of the band structure. Therefore we only consider p orbitals as basis functions in our TB model for the Bi (110) bilayer.

For a Bi (110) bilayer, it is more convenient to use neighboring cells instead of neighboring atoms in the construction of the TB model since this allotrope has a low-symmetry crystal structure and an accurate description of its electronic structure requires inclusion of more neighboring atoms compared to the other two allotropes. In this way, we have used interactions between orbitals in the home cell and orbitals in all eight neighbor cells around it as shown in figure 3(f). For SOC, we have added an on-site intrinsic SOC term to the Hamiltonian similar to our approach for bismuthene. The details of the model's construction are given in appendix A and the values of all hopping parameters and intrinsic SOC strength are listed in table 8.

Table 3. Inversion eigenvalues of occupied states at TRIM for the Bi (110) bilayer. The sign in the bracket denotes parity for non-SOC states.

TRIM\occupied states	1	2	3	4	5	6
(0,0,0)	+(+)	-(-)	+(-)	-(+)	+(+)	-(+)
($\frac{1}{2}$,0,0)	+(+)	-(-)	+(+)	-(-)	+(+)	-(-)
(0, $\frac{1}{2}$,0)	+(+)	-(-)	+(+)	-(-)	+(+)	-(-)
($\frac{1}{2}$, $\frac{1}{2}$,0)	+(+)	+(+)	-(-)	-(-)	-(-)	-(-)

We now proceed to discuss the band structures near the Fermi level. For spinless eigenstates, the electronic bands at Γ consist of mixing between the sets of p_y and p_z orbitals, while mixing of p_x orbitals is disallowed, as shown in the basis function in table 9. After SOC is included, the orbital characters at Γ are a mixture of all p orbitals. The effect of SOC also induces a band inversion at Γ between the two bands at either side of the Fermi level, implying a gap-closing topological phase transition. Interestingly, the band gap sits on the high symmetry line $\Gamma-X_2$ now instead of Γ with a size of 120 meV, yielding two electron pockets along these high symmetry directions while the bands near Γ point are flat. Our orbital character analysis shows that the p_z component dominates in both electron and hole band, which explains the relatively smaller size of the band gap than the Bi (111) bilayer and bismuthene due to a smaller on-site SOC effect for p_z orbitals.

The most notable feature in the electronic bands of the Bi (110) bilayer is the additional degenerate states at X_1 and X_2 due to presence of glide mirror symmetries. For a spinless Hamiltonian, the bands at X_1 and X_2 are doubly degenerate with different in terms of orbital characters. At X_1 , the bands consist of all p orbitals, while at X_2 the mixing between p_x orbitals and other p orbitals is disallowed. The bands at X_1 are doubly degenerate with $\pm C_{2x}$ eigenvalues, while the doubly degenerate bands at X_2 are distinguished by opposite σ_x eigenvalues.

Taking spins into consideration, the orbital characters at X_1 and X_2 are from mixing of the p orbitals across all atoms. The twofold band degeneracy imposed by the glide mirror symmetries is still retained. Then combining with TR and inversion symmetry, the bands will become four-fold degenerate with SOC included. The representations of these fourfold degenerate bands are related to each other by TR and σ_z symmetry. The bands at X_1 and X_2 are all four-fold degenerate with Dirac-like dispersion as a consequence of the effect of non-symmorphic glide mirror symmetries. Such additional degeneracy can be lifted under strong substrate or strain effects. Finally, we calculate inversion eigenvalues of the occupied states and list them in table 3. $\mathbb{Z}_2 = 1$ indicates Bi (110) bilayer is a topological insulator with uncommon non-symmorphic symmetry [17].

5. Conclusion

In conclusion, we have constructed tight binding models for three different allotropes of 2D bismuth, namely, the Bi (111) bilayer, bismuthene and the Bi (110) bilayer, by projecting Bloch states calculated from DFT onto localized atomic orbitals as Wannier functions. We have utilized a minimal set of independent hopping parameters in the TB model to represent the energy bands near the Fermi level. These TB models can accurately reproduce the band topology of these three allotropes compared to previous semi-empirical TB models.

In all cases considered here, we find that the crystalline symmetry plays an important role in constructing Wannier-based TB models. We have tailored the form of the TB model to meet the symmetry constraints imposed on each type of bismuth allotrope. These symmetry constraints can eliminate the numerical errors in the Wannier Hamiltonian, leading to a significant reduction in the number of independent TB parameters. These symmetrized TB models can faithfully recover the band representations near the Fermi level for each bismuth allotrope and also help us to understand the physical origin of the nontrivial band topology and perturbation effects in these bismuth allotropes.

In summary, we have shown that TB models of two-dimensional bismuth allotropes can be effectively derived from the Wannier basis. This symmetry-based approach could be conveniently applied to other topologically nontrivial two-dimensional materials such as antimonene and arsenene [44, 45]. Another advantage of these simplified but accurate models is that they can be easily modified to incorporate external factors such as strain, electric and magnetic fields [46, 47]. Moreover, these models can be a cornerstone for designing new topological structures exhibiting exotic quantum transport properties. For example, the TB models proposed by Su *et al* [48] have inspired experimental realization of stable topological quantum states in graphene nanoribbons [49]. Therefore we expect our simplified and symmetrized TB models could

play a critical role in multi-scale modeling of low-dimensional topological structures, potentially offering an accurate picture of device physics at lowered computational cost [23].

Acknowledgments

The authors acknowledge the support of the Australian Research Council Centre of Excellence in Future Low-Energy Electronics Technologies. (CE170100039). The authors also acknowledge the support from Australian National Computing Infrastructure and Pawsey Supercomputing Centre. MVK acknowledges the support of the Australian Research Council Centre of Excellence in Exciton Science (CE170100026).

Data availability statement

The data that support the findings of this study are available upon reasonable request from the authors.

Appendix A

A.1. Lattice vectors and atomic coordinates

In this section, we give coordinates of unit cell lattice vectors, atomic coordinates and hopping vectors of Bi (111) bilayer, bismuthene and Bi (110) bilayer as defined in figure 3. The unit cell lattice vectors (a_1, a_2) are given in the form of Cartesian coordinates in terms of the lattice parameter (a for Bi (111) bilayer and bismuthene, a and b for Bi (110) bilayer). The atomic coordinates (τ_i) are given as fractional coordinates with respect to a_1 and a_2 . For Bi (110) bilayer, a fractional difference (δ) between two layers is used to express the atomic fractional coordinates. The atomic hopping vectors (r_i) for Bi (111) bilayer and bismuthene are given in vector forms in terms of unit cell lattice vectors and atomic vectors.

Bi (111) bilayer.

$$\begin{aligned} a &= 4.33 \text{ \AA}. \\ a_1 &= a\left(\frac{\sqrt{3}}{2}, \frac{1}{2}\right). \\ a_2 &= a\left(-\frac{\sqrt{3}}{2}, \frac{1}{2}\right). \\ \tau_1 &= \left(\frac{1}{3}, \frac{2}{3}\right). \\ \tau_2 &= \left(\frac{1}{3}, \frac{1}{3}\right). \\ r_1 &= \tau_2 - \tau_1. \\ r_2 &= a_2 + \tau_2 - \tau_1. \\ r_3 &= -a_1 + \tau_2 - \tau_1. \\ r_4 &= a_1. \\ r_5 &= a_1 + a_2. \\ r_6 &= a_2. \\ r_7 &= -a_1 - a_2 + \tau_2 - \tau_1. \\ r_8 &= -a_1 + a_2 + \tau_2 - \tau_1. \\ r_9 &= a_1 + a_2 + \tau_2 - \tau_1. \\ r_{10} &= a_1 + 2a_2 + \tau_2 - \tau_1. \\ r_{11} &= 2a_2 + \tau_2 - \tau_1. \\ r_{12} &= -2a_1 + \tau_2 - \tau_1. \\ r_{13} &= -2a_1 - a_2 + \tau_2 - \tau_1. \\ r_{14} &= -a_2 + \tau_2 - \tau_1. \\ r_{15} &= a_1 + \tau_2 - \tau_1 \end{aligned}$$

Bismuthene.

$$\begin{aligned} a &= 5.35 \text{ \AA}. \\ a_1 &= a\left(\frac{\sqrt{3}}{2}, \frac{1}{2}\right). \\ a_2 &= a\left(-\frac{\sqrt{3}}{2}, \frac{1}{2}\right). \\ \tau_1 &= \left(\frac{1}{3}, \frac{2}{3}\right). \\ \tau_2 &= \left(\frac{1}{3}, \frac{1}{3}\right). \\ r_1 &= \tau_2 - \tau_1. \\ r_2 &= a_2 + \tau_2 - \tau_1. \\ r_3 &= -a_1 + \tau_2 - \tau_1. \\ r_4 &= a_1. \\ r_5 &= a_1 + a_2. \\ r_6 &= a_2. \end{aligned}$$

Bi (110) bilayer.

$$\begin{aligned}a &= 4.56 \text{ \AA}. \\b &= 4.87 \text{ \AA}. \\a_1 &= a(1, 0). \\a_2 &= b(0, 1). \\\delta &= 0.037. \\\tau_1 &= (0, \frac{1}{2} - \delta). \\\tau_2 &= (\frac{1}{2}, 1 - \delta). \\\tau_3 &= (0, \frac{1}{2} + \delta). \\\tau_4 &= (\frac{1}{2}, \delta).\end{aligned}$$

A.2. Details of constructing TB models for bismuth allotropes*A.2.1. Spinless real-space Hamiltonian of a Bi (111) bilayer*

Here, we present how to generate a real-space Hamiltonian from the interaction effect of symmetries operations on atomic orbitals and lattice sites. The crystal structure of a Bi (111) bilayer has the D_{3d} point group symmetry. The symmetry constraints on the real-space basis function include identity (E), inversion (I), three-fold rotation (C_3) and mirror symmetry (σ). We can write down the matrix representation of these symmetry operations on a set of p orbital basis $\{p_z, p_x, p_y\}$ from the same atom:

$$\begin{aligned}D(E) &= \begin{pmatrix} 1 & 0 & 0 \\ 0 & 1 & 0 \\ 0 & 0 & 1 \end{pmatrix} \\D(I) &= \begin{pmatrix} -1 & 0 & 0 \\ 0 & -1 & 0 \\ 0 & 0 & -1 \end{pmatrix} \\D(C_3^+) &= \begin{pmatrix} 1 & 0 & 0 \\ 0 & -\frac{1}{2} & \frac{\sqrt{3}}{2} \\ 0 & -\frac{\sqrt{3}}{2} & -\frac{1}{2} \end{pmatrix} \\D(\sigma_{110}) &= \begin{pmatrix} 1 & 0 & 0 \\ 0 & 1 & 0 \\ 0 & 0 & -1 \end{pmatrix}.\end{aligned}$$

Other symmetry elements can be generated using:

$$S_6^+ = iC_3^-$$

$$S_6^- = iC_3^+$$

$$\sigma_{010} = \sigma_{110}C_3^-$$

$$\sigma_{100} = \sigma_{110}C_3^+$$

$$C_2^{010} = i\sigma_{010}$$

$$C_2^{100} = i\sigma_{100}$$

$$C_2^{110} = i\sigma_{110}.$$

We also introduce matrices to describe the symmetry operations on lattice sites. In the primitive cell of Bi (111) bilayer, there are two atoms. We can therefore write these operations as 2×2 matrices in the basis of lattice sites 1, 2 as:

$$\begin{aligned}D(E) &= \begin{pmatrix} 1 & 0 \\ 0 & 1 \end{pmatrix} \\D(C_3^+) &= \begin{pmatrix} 1 & 0 \\ 0 & 1 \end{pmatrix}\end{aligned}$$

Table 4. Hopping parameters for Bi (111) bilayer, up to and including fourth NN. Parameters with an asterisk superscript are related with other parameters in the table and they can be calculated by equations (36)–(38) in the appendix A.

Parameter	Energy (eV)	Parameter	Energy (eV)
t_1	-2.762	t_9	0.160
t_2	-2.461	t_{10}	-0.226*
t_3	0.292	t_{11}	0.211
t_4	-1.078	t_{12}	-0.014
t_5	1.238	t_{13}	-0.072*
t_6	-0.462	t_{14}	0.287*
t_7	-0.002	t_{15}	0.054
t_8	0.175		
t_{16}	0.052	t_{22}	-0.037
t_{17}	0.001	t_{23}	0.022
t_{18}	0.002*	t_{24}	-0.046
t_{19}	-0.041	t_{25}	0.010
t_{20}	-0.004*	t_{26}	0.021
t_{21}	-0.046	t_{27}	-0.025
λ	1.300		
λ_1	0.013	λ_4	0.010
λ_2	-0.025	λ_5	-0.028
λ_3	0.005	λ_6	0.021

$$D(i) = \begin{pmatrix} 0 & 1 \\ 1 & 0 \end{pmatrix}$$

$$D(\sigma_{110}) = \begin{pmatrix} 0 & 1 \\ 1 & 0 \end{pmatrix}.$$

We can obtain the form of real-space spinless Hamiltonian by equation (5). The $D(g)$ matrices in the equation (5) are 6×6 matrices as a result of the tensor product between orbital representation matrices and lattice site representation matrices. In addition, the real-space Hamiltonian should be Hermitian:

$$H_R = H_{-R}^\dagger, \quad (11)$$

where R is a lattice vector. This can be derived from a Fourier transform of the Bloch Hamiltonian.

In the following, we give the form of different real-space Hamiltonians of a Bi (111) bilayer by considering up to 4th atomic neighbors in detail. The basis set is $\{p_z^{(1)}, p_x^{(1)}, p_y^{(1)}, p_z^{(2)}, p_x^{(2)}, p_y^{(2)}\}$ where (1) and (2) denote each of the two atoms in the primitive cell, as labeled in figure 3(c). Then each real-space Hamiltonian consists of $4 \times 3 \times 3$ sub-blocks corresponding to four possible ways of hoppings between two lattice sites. Therefore we can analyze different atomic neighbor hopping by focusing on specific sub-blocks of a real-space Hamiltonian. The hopping terms in all real-space Hamiltonians are significantly constrained by symmetry operations. These terms are given in table 4.

First, for investigating the on-site and the nearest atomic neighbor hoppings, we derive the real space Hamiltonian for the home cell [000]:

$$H_{[000]} = \begin{pmatrix} t_1 & 0 & 0 & t_3 & t_4 & 0 \\ 0 & t_2 & 0 & t_4 & t_5 & 0 \\ 0 & 0 & t_2 & 0 & 0 & t_6 \\ t_3 & t_4 & 0 & t_1 & 0 & 0 \\ t_4 & t_5 & 0 & 0 & t_2 & 0 \\ 0 & 0 & t_6 & 0 & 0 & t_2 \end{pmatrix}. \quad (12)$$

The diagonal sub-blocks are on-site hoppings while the off-diagonal sub-blocks are hopping between lattice sites in neighboring cells and the home cell. In the diagonal sub-blocks, C_3 , σ , and Hermiticity lead to non-zero hopping terms in the diagonal entries of $H_{[000]}$. As the two lattice sites are related by inversion symmetry, the two diagonal sub-blocks should have the same form, resulting in the only independent parameters in the diagonal sub-blocks to be t_1 and t_2 . Similarly, for the off-diagonal sub-blocks, the symmetry constraints also limit the number of independent parameters to four. Consequently, $H_{[000]}$ can be written with only six independent hopping terms.

We now analyze the form of next-nearest atomic neighbor hopping terms by examining the interactions between the home cell $R = [000]$ and the cell at $R = [100]$. There are also four types of hopping terms here:

hopping from lattice site 1 (2) in home cell to lattice site 1 (2) in the cell at $\mathbf{R} = [100]$. The real-space Hamiltonian of cell $\mathbf{R} = [100]$ is expressed in the form:

$$H_{[100]} = \begin{pmatrix} t_7 & t_8 & t_9 & 0 & 0 & 0 \\ t_{10} & t_{11} & t_{12} & 0 & 0 & 0 \\ t_{13} & t_{14} & t_{15} & 0 & 0 & 0 \\ 0 & 0 & 0 & t_7 & t_{10} & t_{13} \\ 0 & 0 & 0 & t_8 & t_{11} & t_{14} \\ 0 & 0 & 0 & t_9 & t_{12} & t_{15} \end{pmatrix}. \quad (13)$$

By applying mirror symmetry $\sigma_{(100)}$ and Hermiticity, further constraints can be found on $H_{[100]}$:

$$t_{10} = -\frac{1}{2}t_8 - \frac{\sqrt{3}}{2}t_9 \quad (14)$$

$$t_{13} = \frac{\sqrt{3}}{2}t_8 + \frac{1}{2}t_9 \quad (15)$$

$$t_{14} = \sqrt{3}t_{11} - t_{12} - \sqrt{3}t_{15}. \quad (16)$$

Hence there are only six independent parameters in the next-nearest neighbor part of $H_{[100]}$. The off-diagonal blocks are zero since we only include the terms for next-nearest atomic neighbors here.

As for 3rd atomic neighbor interactions, we use the off-diagonal part of the real-space Hamiltonian of cell $\mathbf{R} = [110]$, which has the form:

$$H_{[110]} = \begin{pmatrix} 0 & 0 & 0 & t_{16} & t_{17} & t_{18} \\ 0 & 0 & 0 & t_{17} & t_{19} & t_{20} \\ 0 & 0 & 0 & t_{18} & t_{20} & t_{21} \\ t_{16} & t_{17} & -t_{18} & 0 & 0 & 0 \\ t_{17} & t_{19} & -t_{20} & 0 & 0 & 0 \\ -t_{18} & -t_{20} & t_{21} & 0 & 0 & 0 \end{pmatrix}. \quad (17)$$

There also exist restrictions on entries in the sub-blocks due to C_2^{010} and Hermiticity. These are:

$$t_{18} = \sqrt{3}t_{17} \quad (18)$$

$$t_{20} = \sqrt{3}(t_{21} - t_{19}). \quad (19)$$

Consequently there are only four independent parameters for 3rd atomic neighbors.

Finally, for 4th atomic neighbor interactions, we look at the off-diagonal terms of H_{100}^4 :

$$H_{100}^4 = \begin{pmatrix} 0 & 0 & 0 & t_{22} & t_{23} & t_{24} \\ 0 & 0 & 0 & t_{23} & t_{25} & t_{26} \\ 0 & 0 & 0 & t_{24} & t_{26} & t_{27} \\ t_{22} & t_{23} & t_{24} & 0 & 0 & 0 \\ t_{23} & t_{25} & t_{26} & 0 & 0 & 0 \\ t_{24} & t_{26} & t_{27} & 0 & 0 & 0 \end{pmatrix}. \quad (20)$$

There are six independent entries in the sub-block of the real-space Hamiltonian H_{100}^4 due to inversion symmetry and Hermiticity. The rest of the hopping terms can be generated easily using the other C_2 and C_3^\pm rotations and taking the Hermitian adjoint. Now we have finished construction of spinless Hamiltonian with up to 4th neighbor interaction included using the form of real-space Hamiltonian.

In the following, we list the explicitly how to generate all the hoppings using symmetry operations.

Nearest neighbors:

$$H_{[010]}^{12} = D(C_3^+) H_{[000]}^{12} D^{-1}(C_3^+)$$

$$H_{[100]}^{12} = D(C_3^-) H_{[000]}^{12} D^{-1}(C_3^-)$$

$$H_{[000]}^{21} = H_{[000]}^{12\dagger}$$

$$H_{[0\bar{1}0]}^{21} = D(C_3^+) H_{[000]}^{21} D^{-1}(C_3^+)$$

$$H_{[100]}^{21} = D(C_3^-) H_{[000]}^{21} D^{-1}(C_3^-).$$

2nd nearest neighbors:

$$\begin{aligned}
 H_{[010]}^{11} &= D(C_3^+) H_{[100]}^{11} D^{-1}(C_3^+) \\
 H_{[\bar{1}\bar{1}0]}^{11} &= D(C_3^-) H_{[100]}^{11} D^{-1}(C_3^-) \\
 H_{[1\bar{1}0]}^{11} &= D(\sigma_{010}) H_{[100]}^{11} D^{-1}(\sigma_{010}) \\
 H_{[\bar{1}00]}^{11} &= D(\sigma_{100}) H_{[100]}^{11} D^{-1}(\sigma_{100}) \\
 H_{[0\bar{1}0]}^{11} &= D(\sigma_{110}) H_{[100]}^{11} D^{-1}(\sigma_{110}) \\
 H_{[100]}^{22} &= H_{[100]}^{11\dagger} \\
 H_{[010]}^{22} &= D(C_3^+) H_{[100]}^{22} D^{-1}(C_3^+) \\
 H_{[\bar{1}\bar{1}0]}^{22} &= D(C_3^-) H_{[100]}^{22} D^{-1}(C_3^-) \\
 H_{[1\bar{1}0]}^{22} &= D(\sigma_{010}) H_{[100]}^{22} D^{-1}(\sigma_{010}) \\
 H_{[\bar{1}00]}^{22} &= D(\sigma_{100}) H_{[100]}^{22} D^{-1}(\sigma_{100}) \\
 H_{[0\bar{1}0]}^{22} &= D(\sigma_{110}) H_{[100]}^{22} D^{-1}(\sigma_{110}).
 \end{aligned}$$

3rd nearest neighbors:

$$\begin{aligned}
 H_{[110]}^{21} &= D(C_2^{[110]}) H_{[110]}^{12} D^{-1}(C_2^{[110]}) \\
 H_{[\bar{1}\bar{1}0]}^{12} &= D(C_3^+) H_{[110]}^{12} D^{-1}(C_3^+) \\
 H_{[\bar{1}\bar{1}0]}^{12} &= D(C_3^-) H_{[110]}^{12} D^{-1}(C_3^-) \\
 H_{[\bar{1}\bar{1}0]}^{21} &= D(C_3^+) H_{[110]}^{21} D^{-1}(C_3^+) \\
 H_{[1\bar{1}0]}^{21} &= D(C_3^-) H_{[110]}^{21} D^{-1}(C_3^-).
 \end{aligned}$$

4th nearest neighbor

$$\begin{aligned}
 H_{[100]}^{21} &= D(i) H_{[100]}^{12} D^{-1}(i) \\
 H_{[020]}^{12} &= D(C_3^+) H_{[100]}^{12} D^{-1}(C_3^+) \\
 H_{[020]}^{21} &= D(S_6^-) H_{[100]}^{12} D^{-1}(S_6^-) \\
 H_{[\bar{2}\bar{1}0]}^{12} &= D(C_3^-) H_{[100]}^{12} D^{-1}(S_6^-) \\
 H_{[210]}^{21} &= D(S_6^+) H_{[100]}^{12} D^{-1}(S_6^+) \\
 H_{[010]}^{21} &= D(C_2^{[110]}) H_{[100]}^{12} D^{-1}(C_2^{[110]}) \\
 H_{[0\bar{1}0]}^{12} &= D(\sigma_{110}) H_{[100]}^{12} D^{-1}(\sigma_{110}) \\
 H_{[200]}^{21} &= D(C_2^{[100]}) H_{[100]}^{12} D^{-1}(C_2^{[100]}) \\
 H_{[\bar{2}00]}^{12} &= D(\sigma_{100}) H_{[100]}^{12} D^{-1}(\sigma_{100}) \\
 H_{[\bar{1}\bar{2}0]}^{21} &= D(C_2^{[010]}) H_{[100]}^{12} D^{-1}(C_2^{[010]}) \\
 H_{[120]}^{12} &= D(\sigma_{010}) H_{[100]}^{12} D^{-1}(\sigma_{010}).
 \end{aligned}$$

A.2.2. Spinless k -space Hamiltonian of a Bi (111) bilayer

The k -space TB Hamiltonian can then be constructed from the real-space Hamiltonian using equation (3). We use a convention where the real-space Hamiltonian is dependent on the lattice vectors \mathbf{R} and sublattice vectors $\boldsymbol{\tau}_\alpha$ and $\boldsymbol{\tau}_\beta$ that correspond to particular atomic sites. We construct hopping parameters within a group of NN interactions by applying symmetry operations to the Hamiltonian (which in turn depends on \mathbf{R} , $\boldsymbol{\tau}_\alpha$, and $\boldsymbol{\tau}_\beta$).

It is thereby possible to generate all hopping vectors within a given set of NN interactions (i.e. first, second, third, or fourth, as shown in figure 3(a)) from the interactions between one pair of neighbor atoms in the set. We denote \mathbf{r}_1 to \mathbf{r}_3 as nearest neighbor hopping vectors, \mathbf{r}_4 to \mathbf{r}_6 as second-nearest neighbor hopping vectors, \mathbf{r}_7 to \mathbf{r}_9 as third-nearest neighbor hopping vectors, and \mathbf{r}_{10} to \mathbf{r}_{15} as fourth-nearest neighbor hopping vectors. The symmetry operations not only generate hopping parameters but also enforce the symmetry constraints that are defined in equations (5) and (6).

The k -space TB Hamiltonian consists of sub-blocks related to hoppings between two sublattice atoms as shown in equation (21):

$$H(\mathbf{k}) = \begin{pmatrix} H^{11}(\mathbf{k}) & H^{12}(\mathbf{k}) \\ H^{21}(\mathbf{k}) & H^{22}(\mathbf{k}) \end{pmatrix}. \quad (21)$$

Here we use the superscript to denote interactions between atoms and subscript for interactions between orbitals in Hamiltonian H . The diagonal blocks $H^{11}(\mathbf{k})$ and $H^{22}(\mathbf{k})$ are on-site energies of the two bismuth atoms (Bi1 and Bi2) in the home cell, while $H^{12}(\mathbf{k})$ and $H^{21}(\mathbf{k})$ are hopping matrix between the two bismuth atoms. The matrix elements in every $H^{ij}(\mathbf{k})$ are therefore denoted as $H_{ij}(\mathbf{k})$, which represents the interactions between orbitals. The indices 1, 2, ..., 6 correspond to the orbitals $\{p_{z\text{Bi}1}, p_{x\text{Bi}1}, p_{y\text{Bi}1}, p_{z\text{Bi}2}, p_{x\text{Bi}2}, p_{y\text{Bi}2}\}$. We have dropped k dependence in the sub-blocks for brevity:

$$H^{11}(\mathbf{k}) = \begin{pmatrix} H_{11} & H_{12} & H_{13} \\ & H_{22} & H_{23} \\ \text{h.c.} & & H_{33} \end{pmatrix} \quad (22)$$

$$H^{12}(\mathbf{k}) = \begin{pmatrix} H_{14} & H_{15} & H_{16} \\ H_{15} & H_{25} & H_{26} \\ H_{16} & H_{26} & H_{36} \end{pmatrix}. \quad (23)$$

$H^{22}(\mathbf{k})$ and $H^{21}(\mathbf{k})$ can be obtained by applying an inversion operation to $H^{11}(\mathbf{k})$ and Hermit adjoint to $H^{12}(\mathbf{k})$ respectively:

$$H^{22}(\mathbf{k}) = H^{11}(-\mathbf{k}) \quad (24)$$

$$H^{12}(\mathbf{k}) = H^{21}(\mathbf{k})^\dagger. \quad (25)$$

Constrained by the inversion symmetry and Hermitian condition, $H^{12}(\mathbf{k})$ is symmetric. Hence, we only need to solve for $H^{11}(\mathbf{k})$ and $H^{12}(\mathbf{k})$. $H_{ii}(\mathbf{k})$ represents the self-interaction energy of an orbital with itself, which can be expressed as:

$$H_{ii}(\mathbf{k}) = \epsilon_i + 2h_{ii}^{(1)}[\cos(\mathbf{k} \cdot \mathbf{r}_4) + \cos(\mathbf{k} \cdot \mathbf{r}_6)] + 2h_{ii}^{(2)} \cos(\mathbf{k} \cdot \mathbf{r}_5), \quad (26)$$

where $\epsilon_1, \epsilon_2, \epsilon_3 = t_1, t_2, t_2$; $h_{11}^{(1)}, h_{22}^{(1)}, h_{33}^{(1)} = t_7, t_{11}, t_{15}$; $h_{11}^{(2)}, h_{22}^{(2)}, h_{33}^{(2)} = t_7, (\frac{3}{2}t_{15} - \frac{1}{2}t_{11}), (\frac{3}{2}t_{11} - \frac{1}{2}t_{15})$. Here t_i denote real space hopping parameters as defined in equation (4).

For the remaining off-diagonal elements $H^{11}(\mathbf{k})$, they are given by:

$$H_{12}(\mathbf{k}) = 2ih_{12}^{(1)} \sin(\mathbf{k} \cdot \mathbf{r}_5) + h_{12}^{(2)}(e^{i\mathbf{k} \cdot \mathbf{r}_4} + e^{-i\mathbf{k} \cdot \mathbf{r}_6}) + h_{12}^{(3)}(e^{-i\mathbf{k} \cdot \mathbf{r}_4} + e^{i\mathbf{k} \cdot \mathbf{r}_6}) \quad (27)$$

$$H_{13}(\mathbf{k}) = 2ih_{13}^{(1)} \sin(\mathbf{k} \cdot \mathbf{r}_5) + h_{13}^{(2)}(e^{i\mathbf{k} \cdot \mathbf{r}_4} - e^{-i\mathbf{k} \cdot \mathbf{r}_6}) + h_{13}^{(3)}(e^{-i\mathbf{k} \cdot \mathbf{r}_4} - e^{i\mathbf{k} \cdot \mathbf{r}_6}) \quad (28)$$

$$H_{23}(\mathbf{k}) = 2ih_{23}^{(1)} \sin(\mathbf{k} \cdot \mathbf{r}_5) + h_{23}^{(2)}(e^{i\mathbf{k} \cdot \mathbf{r}_4} - e^{-i\mathbf{k} \cdot \mathbf{r}_6}) + h_{23}^{(3)}(e^{-i\mathbf{k} \cdot \mathbf{r}_4} - e^{i\mathbf{k} \cdot \mathbf{r}_6}), \quad (29)$$

where the constants $h_{ij}^{(m)}$ are related to hopping parameters by: $h_{12}^{(1)} = (-\frac{1}{2}t_8 + \frac{\sqrt{3}}{2}t_9)$, $h_{12}^{(2)} = t_8$, $h_{12}^{(3)} = (-\frac{1}{2}t_8 - \frac{\sqrt{3}}{2}t_9)$, $h_{13}^{(1)} = (\frac{1}{2}t_8 + \frac{\sqrt{3}}{2}t_9)$, $h_{13}^{(2)} = t_9$, $h_{13}^{(3)} = (-\frac{\sqrt{3}}{2}t_8 + \frac{1}{2}t_9)$, $h_{23}^{(1)} = (\frac{1}{2}t_{14} - \frac{1}{2}t_{12})$, $h_{23}^{(2)} = t_{12}$, and $h_{23}^{(3)} = t_{14}$ respectively.

For off-diagonal hopping sub-block $H^{12}(\mathbf{k})$, the matrix elements can be similarly expressed as:

$$H_{14}(\mathbf{k}) = h_{14}^{(1)}(e^{i\mathbf{k} \cdot \mathbf{r}_1} + e^{i\mathbf{k} \cdot \mathbf{r}_2} + e^{i\mathbf{k} \cdot \mathbf{r}_3}) \quad (30)$$

$$H_{15}(\mathbf{k}) = h_{15}^{(1)} \left(e^{i\mathbf{k} \cdot \mathbf{r}_1} - \frac{1}{2} e^{i\mathbf{k} \cdot \mathbf{r}_2} - \frac{1}{2} e^{i\mathbf{k} \cdot \mathbf{r}_3} \right) \quad (31)$$

$$H_{16}(\mathbf{k}) = h_{16}^{(1)}(e^{i\mathbf{k} \cdot \mathbf{r}_2} - e^{i\mathbf{k} \cdot \mathbf{r}_3}) \quad (32)$$

$$H_{25}(\mathbf{k}) = h_{25}^{(1)} e^{i\mathbf{k} \cdot \mathbf{r}_1} + h_{25}^{(2)} e^{i\mathbf{k} \cdot \mathbf{r}_2} + h_{25}^{(2)} e^{i\mathbf{k} \cdot \mathbf{r}_3} \quad (33)$$

$$H_{26}(\mathbf{k}) = h_{26}^{(1)} e^{i\mathbf{k} \cdot \mathbf{r}_2} - h_{26}^{(1)} e^{i\mathbf{k} \cdot \mathbf{r}_2} \quad (34)$$

$$H_{36}(\mathbf{k}) = h_{36}^{(1)} e^{i\mathbf{k} \cdot \mathbf{r}_1} + h_{36}^{(2)} e^{i\mathbf{k} \cdot \mathbf{r}_2} + h_{36}^{(2)} e^{i\mathbf{k} \cdot \mathbf{r}_3}. \quad (35)$$

Again, $h_{14}^{(1)} = t_3$, $h_{15}^{(1)} = t_4$, $h_{25}^{(1)} = t_5$, $h_{25}^{(2)} = (\frac{1}{4}t_5 + \frac{3}{4}t_6)$, $h_{26}^{(1)} = (-\frac{\sqrt{3}}{4}t_5 + \frac{\sqrt{3}}{4}t_6)$, $h_{36}^{(1)} = t_6$ and $h_{36}^{(2)} = (\frac{3}{4}t_5 + \frac{1}{4}t_6)$.

Following this procedure, we obtain the spinless TB Hamiltonian with 12 independent parameters (t_1 to t_{15} , except t_{10} , t_{13} and t_{14}) for Bi (111) bilayer with up to the next-nearest neighbor interactions as summarized in table 4. If one desires a better description of the CBs, third and fourth NN interactions can be included. As shown in table 4, a TB model involving up to four NN interactions included needs 10 additional independent hopping parameters (t_{16} to t_{27} , except t_{18} and t_{20}). In the appendix A, we discuss the symmetry constraints imposed on the real space Hamiltonian and give the explicit forms of the real space Hamiltonian up to fourth NN interactions.

A.2.3. Symmetry constraints on SOC for the Bi (111) bilayer and basis functions of IRs

In the Bi (111) bilayer we consider two types of SOC terms, namely on-site SOC and a next-nearest atomic neighbor SOC referred to as intrinsic. The on-site SOC can be directly calculated using the expanded form of equation (8):

$$H_{\text{soc}} = \lambda \frac{\hat{L}_- \hat{S}_+ + \hat{L}_+ \hat{S}_-}{2} + \hat{L}_z \hat{S}_z. \quad (36)$$

And then the on-site SOC matrix has the form:

$$H_{\text{soc}} = \begin{pmatrix} 0 & 0 & 0 & 0 & 0 & 0 & 0 & -1 & i & 0 & 0 & 0 \\ 0 & 0 & -i & 0 & 0 & 0 & 1 & 0 & 0 & 0 & 0 & 0 \\ 0 & i & 0 & 0 & 0 & 0 & -i & 0 & 0 & 0 & 0 & 0 \\ 0 & 0 & 0 & 0 & 0 & 0 & 0 & 0 & 0 & 0 & -1 & i \\ 0 & 0 & 0 & 0 & 0 & -i & 0 & 0 & 0 & 1 & 0 & 0 \\ 0 & 0 & 0 & 0 & i & 0 & 0 & 0 & 0 & -i & 0 & 0 \\ 0 & 1 & i & 0 & 0 & 0 & 0 & 0 & 0 & 0 & 0 & 0 \\ -1 & 0 & 0 & 0 & 0 & 0 & 0 & 0 & i & 0 & 0 & 0 \\ -i & 0 & 0 & 0 & 0 & 0 & 0 & -i & 0 & 0 & 0 & 0 \\ 0 & 0 & 0 & 0 & 1 & i & 0 & 0 & 0 & 0 & 0 & 0 \\ 0 & 0 & 0 & -1 & 0 & 0 & 0 & 0 & 0 & 0 & 0 & i \\ 0 & 0 & 0 & -i & 0 & 0 & 0 & 0 & 0 & 0 & -i & 0 \end{pmatrix}.$$

Next we turn to the intrinsic SOC. The form of this SOC can be obtained by using the approach in the previous section for deriving hopping terms. The crystal symmetries, TR symmetry and Hermicity play important roles in limiting the number of independent SOC terms.

We can write the next-nearest atomic neighbor SOC hopping terms by investigating the diagonal terms of real-space intrinsic SOC Hamiltonian $H_I[110]$:

$$H_I[110] = i\sigma_z \otimes \begin{pmatrix} H_{I,11}[\bar{1}\bar{1}0] & 0 \\ 0 & H_{I,11}[\bar{1}\bar{1}0]^\dagger \end{pmatrix}, \quad (37)$$

where σ_z is a Pauli matrix and $H_{I,11}[\bar{1}\bar{1}0]$ represents the SOC between atom 1 in the home cell and atom 1 in cell $R = [\bar{1}\bar{1}0]$. $H_{I,11}[\bar{1}\bar{1}0]$ has the form:

$$\begin{pmatrix} \lambda_1 & \lambda_2 & \lambda_3 \\ \lambda_2 & \lambda_4 & \lambda_5 \\ -\lambda_3 & -\lambda_5 & \lambda_6 \end{pmatrix}.$$

Using the findings in the previous section, when the symmetry constraints act on the next-nearest hopping terms, there will only be six independent terms. We can therefore include the contribution of SOC in a Bi (111) bilayer through an on-site SOC strength λ and next-nearest SOC strengths λ_1 to λ_6 .

In table 5, we calculate the general forms of basis functions of each band representations at Γ to assist analysis of band structures.

A.2.4. Real-space Hamiltonian of bismuthene

Applying the same symmetry operations of a (111) bilayer listed in the previous section on the real-space Hamiltonian of Bismuthene, the real-space Hamiltonian including up to NN interactions can be obtained. We describe the electronic structure of bismuthene with nine independent parameters as shown in table 6. The number of hopping terms are reduced by the presence of crystal symmetries and Hermiticity. When considering SOC, the form of on-site SOC Hamiltonian of bismuthene is identical to that of Bi (111) bilayer.

Table 5. Basis functions of IRs at the Γ point for the point group D_{3d} , obtained from the projection operator method [50].

IRs	Basis functions
Γ_1^+	$ p_z^+\rangle$
Γ_3^+	$\{ p_x^+\rangle, p_y^+\rangle\}$
Γ_2^-	$ p_z^-\rangle$
Γ_3^-	$\{ p_x^-\rangle, p_y^-\rangle\}$
Γ_4^+	$\frac{1}{2}(p_x^+\uparrow\rangle + i p_y^+\uparrow\rangle - i p_x^-\downarrow\rangle - p_y^-\downarrow\rangle)$
Γ_5^+	$\frac{1}{2}(p_x^+\uparrow\rangle + i p_y^+\uparrow\rangle + i p_x^-\downarrow\rangle + p_y^-\downarrow\rangle)$
Γ_6^+	$\{ \uparrow \rangle, \downarrow \rangle\}$
Γ_4^-	$\left\{a_+ p_z^+\uparrow\rangle + a_-^-\frac{1}{\sqrt{2}}(p_x^-\downarrow\rangle + i p_y^-\downarrow\rangle), a_+^* p_z^-\downarrow\rangle + a_-^*\frac{1}{\sqrt{2}}(p_x^+\uparrow\rangle - i p_y^+\uparrow\rangle)\right\}$
Γ_5^-	$\frac{1}{2}(p_x^-\uparrow\rangle + i p_y^-\uparrow\rangle - i p_x^-\downarrow\rangle - p_y^-\downarrow\rangle)$
Γ_6^-	$\frac{1}{2}(p_x^-\uparrow\rangle + i p_y^-\uparrow\rangle + i p_x^-\downarrow\rangle + p_y^-\downarrow\rangle)$
	$\left\{a_- p_z^-\uparrow\rangle + a_-^-\frac{1}{\sqrt{2}}(p_x^-\downarrow\rangle + i p_y^-\downarrow\rangle), a_-^* p_z^-\downarrow\rangle + a_-^*\frac{1}{\sqrt{2}}(p_x^-\uparrow\rangle - i p_y^-\uparrow\rangle)\right\}$

Table 6. Hopping parameters for bismuthene, up to and including second NNs. The parameter with an asterisk superscript is related with other parameters in the table.

Parameter	Energy (eV)
t_1	-3.919
t_2	-3.175
t_3	-0.641
t_4	1.943
t_5	-0.724
t_6	0.053
t_7	-0.152
t_8	-0.070
t_9	-0.037 ^a
t_{10}	-0.091
λ	1.158

$${}^a t_9 = \sqrt{3}(t_7 - t_{10}) - t_8.$$

We have found that the third and fourth NN hoppings have negligible contribution to the band structure and the TB model with next-nearest neighbors already shows satisfactory agreement to DFT results. Therefore, we only include up to next-nearest hoppings in the TB model. First we start with Hamiltonian without spin. The basis set we take is $\{p_{z\text{Bi}1}, p_{x\text{Bi}1}, p_{y\text{Bi}1}, p_{z\text{Bi}2}, p_{x\text{Bi}2}, p_{y\text{Bi}2}\}$ where the 1 and 2 subscripts distinguish the sublattice atoms.

Similarly to a Bi (111) bilayer, we give the form of Hamiltonian for cell $R = [000]$ as:

$$H_{[000]} = \begin{pmatrix} t_1 & 0 & 0 & t_3 & 0 & 0 \\ 0 & t_2 & 0 & 0 & t_4 & 0 \\ 0 & 0 & t_2 & 0 & 0 & t_5 \\ t_3 & 0 & 0 & t_1 & 0 & 0 \\ 0 & t_4 & 0 & 0 & t_2 & 0 \\ 0 & 0 & t_5 & 0 & 0 & t_2 \end{pmatrix}. \quad (38)$$

The next-nearest neighbor hopping terms can be obtained by looking at diagonal sub-blocks of $H_{[100]}$:

$$H_{[100]} = \begin{pmatrix} t_6 & 0 & 0 & 0 & 0 & 0 \\ 0 & t_7 & t_8 & 0 & 0 & 0 \\ 0 & t_9 & t_{10} & 0 & 0 & 0 \\ 0 & 0 & 0 & t_6 & 0 & 0 \\ 0 & 0 & 0 & 0 & t_7 & t_8 \\ 0 & 0 & 0 & 0 & t_9 & t_{10} \end{pmatrix}. \quad (39)$$

A.2.5. *k*-space Hamiltonian of bismuthene and basis functions of IRs

Similar to the Bi (111) bilayer, the *k*-space Hamiltonian of bismuthene also consists of four sub-blocks:

$$H(\mathbf{k}) = \begin{pmatrix} H^{11}(\mathbf{k}) & H^{12}(\mathbf{k}) \\ H^{21}(\mathbf{k}) & H^{22}(\mathbf{k}) \end{pmatrix}. \quad (40)$$

Table 7. Basis functions of IRs at Γ point (point group D_{6h}), obtained from projection operator method [50]. There are two sets of p -orbital combinations allowed for Γ^{8+} and Γ^{7-} IRs. The bands with these two IRs consist of linear combination of the in-plane and out-of-plane p -orbitals, in a similar way to Γ^{6+} and Γ^{6-} IRs from D_{3d} group as listed in table 5. The two basis functions within the two dimensional sub-space of these IRs form a Kramer pair conjugated to each other.

Irreducible rep.	Basis functions
Γ_3^+	$ p_z^+\rangle$
Γ_6^+	$\{ p_x^+\rangle, p_y^+\rangle\}$
Γ_2^-	$ p_z^-\rangle$
Γ_5^-	$\{ p_x^-\rangle, p_y^-\rangle\}$
Γ_7^+	$\{ \uparrow\rangle, \downarrow\rangle\}$
Γ_8^+	$\{\frac{1}{\sqrt{2}}(p_x^+\uparrow\rangle - i p_y^+\uparrow\rangle), \frac{1}{\sqrt{2}}(p_x^+\downarrow\rangle + i p_y^+\downarrow\rangle)\}$ $\{ p_x^+\downarrow\rangle, p_z^+\uparrow\rangle\}$
Γ_9^+	$\{\frac{1}{\sqrt{2}}(p_x^+\downarrow\rangle - i p_y^+\downarrow\rangle), \frac{1}{\sqrt{2}}(p_x^+\uparrow\rangle + i p_y^+\uparrow\rangle)\}$
Γ_7^-	$\{\frac{1}{\sqrt{2}}(p_x^-\uparrow\rangle - i p_y^-\uparrow\rangle), \frac{1}{\sqrt{2}}(p_x^-\downarrow\rangle + i p_y^-\downarrow\rangle)\}$ $\{ p_z^-\downarrow\rangle, p_z^-\uparrow\rangle\}$
Γ_9^-	$\{\frac{1}{\sqrt{2}}(p_x^-\downarrow\rangle - i p_y^-\downarrow\rangle), \frac{1}{\sqrt{2}}(p_x^-\uparrow\rangle + i p_y^-\uparrow\rangle)\}$

The form of the sub-blocks are:

$$H^{11}(\mathbf{k}) = \begin{pmatrix} H_{11} & 0 & 0 \\ 0 & H_{22} & H_{23} \\ 0 & H_{32} & H_{33} \end{pmatrix} \quad (41)$$

$$H^{12}(\mathbf{k}) = \begin{pmatrix} H_{14} & 0 & 0 \\ 0 & H_{25} & H_{26} \\ 0 & H_{35} & H_{36} \end{pmatrix}. \quad (42)$$

Again, we only need to solve for $H^{11}(\mathbf{k})$ and $H^{12}(\mathbf{k})$ since the other two sub-blocks can be obtained by inversion and Hermitian adjoint. The $H^{ij}(\mathbf{k})$ of bismuthene has the same components $H_{ij}(\mathbf{k})$ as the Bi (111) bilayer except those zero elements in $H^{11}(\mathbf{k})$ and $H^{22}(\mathbf{k})$, because bismuthene has all the symmetry element generators of Bi (111) bilayer with an extra horizontal mirror symmetry σ_h element. The general form of the on-site hopping term $H_{ii}(\mathbf{k})$ is:

$$H_{ii}(\mathbf{k}) = \epsilon_i + 2h_{ii}^{(1)}[\cos(\mathbf{k} \cdot \mathbf{r}_4) + \cos(\mathbf{k} \cdot \mathbf{r}_6)] + 2h_{ii}^{(2)} \cos(\mathbf{k} \cdot \mathbf{r}_5), \quad (43)$$

where $\epsilon_1, \epsilon_2, \epsilon_3 = t_1, t_2, t_2$; $h_{11}^{(1)}, h_{22}^{(1)}, h_{33}^{(1)} = t_6, t_7, t_{10}$; $h_{11}^{(2)}, h_{22}^{(2)}, h_{33}^{(2)} = t_6, (\frac{3}{2}t_{10} - \frac{1}{2}t_7), (\frac{3}{2}t_7 - \frac{1}{2}t_{10})$ respectively. The only off-diagonal term $H_{23}(\mathbf{k})$ in $H^{11}(\mathbf{k})$ has the form:

$$H_{23}(\mathbf{k}) = 2ih_{23}^{(1)} \sin(\mathbf{k} \cdot \mathbf{r}_5) + h_{23}^{(2)}(e^{i\mathbf{k} \cdot \mathbf{r}_4} - e^{-i\mathbf{k} \cdot \mathbf{r}_6}) + h_{23}^{(3)}(e^{-i\mathbf{k} \cdot \mathbf{r}_4} - e^{i\mathbf{k} \cdot \mathbf{r}_6}), \quad (44)$$

where the constants $h_{23}^{(1)} = (\frac{1}{2}t_9 - \frac{1}{2}t_8)$, $h_{23}^{(2)} = t_8$, and $h_{23}^{(3)} = t_9$. For off-diagonal hopping sub-block $H^{12}(\mathbf{k})$, the components are given by:

$$H_{14}(\mathbf{k}) = h_{14}^{(1)}(e^{i\mathbf{k} \cdot \mathbf{r}_1} + e^{i\mathbf{k} \cdot \mathbf{r}_2} + e^{i\mathbf{k} \cdot \mathbf{r}_3}) \quad (45)$$

$$H_{25}(\mathbf{k}) = h_{25}^{(1)} e^{i\mathbf{k} \cdot \mathbf{r}_1} + h_{25}^{(2)} e^{i\mathbf{k} \cdot \mathbf{r}_2} + h_{25}^{(2)} e^{i\mathbf{k} \cdot \mathbf{r}_3} \quad (46)$$

$$H_{26}(\mathbf{k}) = h_{26}^{(1)} e^{i\mathbf{k} \cdot \mathbf{r}_2} - h_{26}^{(1)} e^{i\mathbf{k} \cdot \mathbf{r}_3} \quad (47)$$

$$H_{35}(\mathbf{k}) = h_{35}^{(1)} e^{i\mathbf{k} \cdot \mathbf{r}_2} - h_{35}^{(1)} e^{i\mathbf{k} \cdot \mathbf{r}_3} \quad (48)$$

$$H_{36}(\mathbf{k}) = h_{36}^{(1)} e^{i\mathbf{k} \cdot \mathbf{r}_1} + h_{36}^{(2)} e^{i\mathbf{k} \cdot \mathbf{r}_2} + h_{36}^{(2)} e^{i\mathbf{k} \cdot \mathbf{r}_3}. \quad (49)$$

Again, $h_{14}^{(1)} = t_3$, $h_{25}^{(1)} = t_4$, $h_{25}^{(2)} = (\frac{1}{4}t_4 + \frac{3}{4}t_5)$, $h_{35}^{(1)} = h_{26}^{(1)} = (-\frac{\sqrt{3}}{4}t_4 + \frac{\sqrt{3}}{4}t_5)$, $h_{36}^{(1)} = t_5$ and $h_{36}^{(2)} = (\frac{3}{4}t_4 + \frac{1}{4}t_5)$. Finally, we obtain 9 independent hopping parameters as shown in table 6.

In table 7, we also give the form of basis functions for each band representations.

A.2.6. Constructing Hamiltonian of Bi (110) bilayer and basis function of IRs

The real-space Hamiltonian matrix describes hopping between the home cell and neighbor cells at \mathbf{R} . The entries of the Hamiltonian can be divided into 16 sub-blocks to represent hopping between four inequivalent atoms in the primitive cells. Therefore, we analyze the form of the real-space Hamiltonian in the unit of a sub-block. For hopping in the home cell $H_{[000]}$, there are 4 independent sub-blocks in the

Table 8. Hopping parameters for the Bi (110) bilayer, up to and including the nearest cells to the home cell.

Parameter	Energy (eV)	Parameter	Energy (eV)
t_1	-2.375	t_{19}	0.063
t_2	-2.075	t_{20}	0.051
t_3	-2.183	t_{21}	-0.111
t_4	-0.080	t_{22}	0.038
t_5	1.766	t_{23}	0.041
t_6	-0.501	t_{24}	-0.084
t_7	-0.453	t_{25}	-0.301
t_8	-0.284	t_{26}	0.376
t_9	-0.573	t_{27}	0.657
t_{10}	0.847	t_{28}	0.019
t_{11}	0.529	t_{29}	0.016
t_{12}	1.232	t_{30}	0.774
t_{13}	-0.031	t_{31}	0.036
t_{14}	0.026	t_{32}	0.072
t_{15}	0.038	t_{33}	0.048
t_{16}	0.064	t_{34}	0.016
t_{17}	0.031	t_{35}	0.014
t_{18}	-0.056	λ	1.240

Hamiltonian: $H_{[000]}^{11}$, $H_{[000]}^{12}$, $H_{[000]}^{13}$ and $H_{[000]}^{14}$. The other sub-blocks can be derived from these independent sub-blocks by applying $\sigma_{(001)}$, inversion, and $C_2^{[001]}$ operations. Symmetries also restrict the number of independent parameters in each sub-block. Finally we can write the hopping in the home cell as:

$$H_{[000]} = \begin{pmatrix} H_{[000]}^{11} & H_{[000]}^{12} & H_{[000]}^{13} & H_{[000]}^{14} \\ \sigma_z(H_{[000]}^{11}) & C_{2y}(H_{[000]}^{14}) & 0 & 0 \\ i(H_{[000]}^{11}) & C_{2x}(H_{[000]}^{12}) & C_{2x}(H_{[000]}^{11}) & C_{2x}(H_{[000]}^{11}) \\ h.c. & & & \end{pmatrix}.$$

Next, we consider hoppings from the home cell to cell $R = [100]$. There are only two independent sub-blocks $H_{[100]}^{11}$ and $H_{[100]}^{24}$:

$$H_{[100]} = \begin{pmatrix} H_{[100]}^{11} & 0 & 0 & 0 \\ \sigma_x(H_{[000]}^{12\dagger}) & \sigma_z(H_{[100]}^{11}) & \sigma_x(H_{[000]}^{23}) & H_{[100]}^{24} \\ 0 & 0 & C_{2x}(H_{[100]}^{11}) & 0 \\ \sigma_y(H_{[000]}^{14}) & C_{2x}(H_{[100]}^{24}) & i(H_{[000]}^{21}) & \sigma_y(H_{[100]}^{11\dagger}) \end{pmatrix}.$$

Similarly for hopping to cell $R = [010]$, $R = [110]$ and $R = [1\bar{1}0]$, we have:

$$H_{[010]} = \begin{pmatrix} H_{[010]}^{11} & 0 & 0 & H_{[010]}^{14} \\ C_{2y}(H_{[000]}^{12}) & C_{2y}(H_{[010]}^{11}) & C_{2y}(H_{[010]}^{14}) & C_{2y}(H_{[000]}^{13}) \\ 0 & 0 & i(H_{[010]}^{11\dagger}) & C_{2z}(H_{[000]}^{21}) \\ 0 & 0 & 0 & \sigma_z(H_{[010]}^{33}) \end{pmatrix}$$

$$H_{[110]} = \begin{pmatrix} H_{[110]}^{11} & 0 & 0 & 0 \\ \sigma_z(H_{[000]}^{12}) & \sigma_z(H_{[110]}^{11}) & \sigma_x(H_{[010]}^{23}) & 0 \\ \sigma_y(H_{[100]}^{24}) & 0 & i(H_{[110]}^{11\dagger}) & 0 \\ 0 & 0 & 0 & \sigma_z(H_{[110]}^{33}) \end{pmatrix}$$

$$H_{[1\bar{1}0]} = \begin{pmatrix} C_{2x}(H_{[110]}^{33}) & 0 & C_{2x}(H_{[110]}^{31}) & 0 \\ 0 & C_{2x}(H_{[110]}^{44}) & 0 & 0 \\ 0 & 0 & C_{2x}(H_{[110]}^{11}) & 0 \\ C_{2x}(H_{[110]}^{23}) & 0 & C_{2x}(H_{[110]}^{21}) & C_{2x}(H_{[110]}^{22}) \end{pmatrix}.$$

The rest of the hoppings to cells at $R = [\bar{1}00]$, $R = [0\bar{1}0]$, $R = [1\bar{1}0]$ and $R = [\bar{1}\bar{1}0]$ can be easily obtain by the Hermitian condition $H(-R) = H(R)^\dagger$. SOC is added by duplicating the basis and directly evaluating matrix elements $\langle w_i | \lambda \hat{L} \cdot \hat{S} | w_j \rangle$ where i and j denote the Wannier orbitals in the home cell and λ is the on-site SOC strength. Table 8 summarizes all the hopping parameters for the Bi (110) bilayer.

The explicit form of the real-space Hamiltonian of cell $R = [uvw]$ still follows the definition as described for the Bi (111) bilayer and bismuthene. For cell $R = [000]$, we write the sub-blocks representing the interactions between one lattice site in the home cell $R = [000]$ and another lattice site in the home cell as,

Table 9. Basis functions of IRs at Γ point for two states near Fermi level, obtained from projection operator method [50].

Irreducible rep.	Basis functions
Γ_2^-	$\frac{1}{2}(p_{y1}\rangle - p_{y2}\rangle + p_{y3}\rangle - p_{y4}\rangle)$ $\frac{1}{2}(p_{z1}\rangle + p_{z2}\rangle + p_{z3}\rangle + p_{z4}\rangle)$
Γ_3^+	$\frac{1}{2}(p_{y1}\rangle - p_{y2}\rangle - p_{y3}\rangle + p_{y4}\rangle)$ $\frac{1}{2}(p_{z1}\rangle + p_{z2}\rangle - p_{z3}\rangle - p_{z4}\rangle)$

Table 10. Basis functions of IRs at Y point, obtained from projection operator method [50].

Irreducible rep.	Basis functions
Y_1	$\{\frac{1}{\sqrt{2}}(p_{y1}\rangle - p_{y3}\rangle), \frac{1}{\sqrt{2}}(p_{y2}\rangle - p_{y4}\rangle)\}$ $\{\frac{1}{\sqrt{2}}(p_{z1}\rangle - p_{z3}\rangle), \frac{1}{\sqrt{2}}(p_{z2}\rangle - p_{z4}\rangle)\}$
Y_2	$\{\frac{1}{\sqrt{2}}(p_{x1}\rangle - p_{x3}\rangle), \frac{1}{\sqrt{2}}(p_{x2}\rangle - p_{x4}\rangle)\}$

Table 11. D_{3d} double group character table.

D_{3d}	E	\bar{E}	$2C_3$	$2\bar{C}_3$	$3C_2'$	$3\bar{C}_2'$	I	\bar{I}	$2S_6$	$2\bar{S}_6$	$3\sigma_d$	$3\bar{\sigma}_d$
Γ_1^+	1	1	1	1	1	1	1	1	1	1	1	1
Γ_2^+	1	1	1	1	-1	-1	1	1	1	1	-1	-1
Γ_3^+	2	2	-1	-1	0	0	2	2	-1	-1	0	0
Γ_1^-	1	1	1	1	1	1	-1	-1	-1	-1	-1	-1
Γ_2^-	1	1	1	1	-1	-1	-1	-1	-1	-1	1	1
Γ_3^-	2	2	-1	-1	0	0	-2	-2	1	1	0	0
Γ_4^+	1	-1	-1	1	i	-i	1	-1	-1	1	i	-i
Γ_5^+	1	-1	-1	1	-i	i	1	-1	-1	1	-i	i
Γ_6^+	2	-2	1	-1	0	0	2	-2	1	-1	0	0
Γ_4^-	1	-1	-1	1	i	-i	-1	1	1	-1	-i	i
Γ_5^-	1	-1	-1	1	-i	i	-1	1	1	-1	i	-i
Γ_6^-	2	-2	1	-1	0	0	-2	2	-1	1	0	0

Table 12. D_{6h} double group character table part 1.

D_{6h}	E	\bar{E}	$\{C_2, \bar{C}_2\}$	$2C_3$	$2\bar{C}_3$	$2C_6$	$2\bar{C}_6$	$\{3C'_2, 3\bar{C}'_2\}$	$\{3C''_2, 3\bar{C}''_2\}$
Γ_1^+	1	1	1	1	1	1	1	1	1
Γ_2^+	1	1	1	1	1	1	1	-1	-1
Γ_3^+	1	1	-1	1	1	-1	-1	1	-1
Γ_4^+	1	1	-1	1	1	-1	-1	-1	1
Γ_5^+	2	2	-2	-1	-1	1	1	0	0
Γ_6^+	2	2	2	-1	-1	-1	-1	0	0
Γ_1^-	1	1	1	1	1	1	1	1	1
Γ_2^-	1	1	1	1	1	1	1	-1	-1
Γ_3^-	1	1	-1	1	1	-1	-1	1	-1
Γ_4^-	1	1	-1	1	1	-1	-1	-1	1
Γ_5^-	2	2	-2	-1	-1	1	1	0	0
Γ_6^-	2	2	2	-1	-1	-1	-1	0	0
Γ_7^+	2	-2	0	1	-1	$\sqrt{3}$	$-\sqrt{3}$	0	0
Γ_8^+	2	-2	0	1	-1	$-\sqrt{3}$	$\sqrt{3}$	0	0
Γ_9^+	2	-2	0	-2	2	0	0	0	0
Γ_7^-	2	-2	0	1	-1	$\sqrt{3}$	$-\sqrt{3}$	0	0
Γ_8^-	2	-2	0	1	-1	$-\sqrt{3}$	$\sqrt{3}$	0	0
Γ_9^-	2	-2	0	-2	2	0	0	0	0

with superscript indicating the sublattice sites and subscript the cell that interacts with the home cell:

$$H_{[000]}^{11} = \begin{pmatrix} t_1 & 0 & t_4 \\ 0 & t_2 & 0 \\ t_4 & 0 & t_3 \end{pmatrix} \quad (50)$$

$$H_{[000]}^{12} = \begin{pmatrix} t_{13} & t_{16} & t_{17} \\ t_{18} & t_{14} & t_{19} \\ 0 & 0 & t_{15} \end{pmatrix} \quad (51)$$

Table 13. D_{6h} double group character table part 2.

D_{6h}	I	\bar{I}	$\{\sigma_h, \bar{\sigma}_h\}$	$2S_6$	$2\bar{S}_6$	$2S_3$	$2\bar{S}_3$	$\{3\sigma_d, 3\bar{\sigma}_d\} \{3\sigma_v, 3\bar{\sigma}_v\}$
Γ_1^+	1	1	1	1	1	1	1	1
Γ_2^+	1	1	1	1	1	1	-1	-1
Γ_3^+	1	1	-1	1	1	-1	-1	1
Γ_4^+	1	1	-1	1	1	-1	-1	1
Γ_5^+	2	2	-2	-1	-1	1	1	0
Γ_6^+	2	2	2	-1	-1	-1	0	0
Γ_1^-	-1	-1	-1	-1	-1	-1	-1	-1
Γ_2^-	-1	-1	-1	-1	-1	-1	1	1
Γ_3^-	-1	-1	1	-1	-1	1	-1	1
Γ_4^-	-1	-1	1	-1	-1	1	1	-1
Γ_5^-	-2	-2	2	1	1	-1	-1	0
Γ_6^-	-2	-2	-2	1	1	1	0	0
Γ_7^+	2	-2	0	1	-1	$\sqrt{3}$	$-\sqrt{3}$	0
Γ_8^+	2	-2	0	1	-1	$-\sqrt{3}$	$\sqrt{3}$	0
Γ_9^+	2	-2	0	-2	2	0	0	0
Γ_7^-	-2	2	0	-1	1	$-\sqrt{3}$	$\sqrt{3}$	0
Γ_8^-	-2	2	0	-1	1	$\sqrt{3}$	$-\sqrt{3}$	0
Γ_9^-	-2	2	0	2	-2	0	0	0

Table 14. D_{2h} double space group character table $u = (\frac{1}{2}, \frac{1}{2}, 0)$.

D_{2h}	E	\bar{E}	$\{C_{2x}, C_{2x}\}$	$\{\{C_{2z} u\}, \{C_{2z} u\}\}$	$\{\{C_{2y} u\}, \{C_{2y} u\}\}$	I	\bar{I}	$\{\sigma_x, \bar{\sigma}_x\}$	$\{\{\sigma_z u\}, \{\bar{\sigma}_z u\}\}$	$\{\{\sigma_y u\}, \{\bar{\sigma}_y u\}\}$
Γ_1^+	1	1	1	1	1	1	1	1	1	1
Γ_2^+	1	1	-1	1	-1	1	1	-1	1	-1
Γ_3^+	1	1	1	-1	-1	1	1	1	-1	-1
Γ_4^+	1	1	-1	-1	1	1	1	-1	-1	1
Γ_1^-	1	1	1	1	1	-1	-1	-1	-1	-1
Γ_2^-	1	1	-1	1	-1	-1	-1	1	-1	1
Γ_3^-	1	1	1	-1	-1	-1	-1	-1	1	1
Γ_4^-	1	1	-1	-1	1	-1	-1	1	1	-1
Γ_5^+	2	-2	0	0	0	2	-2	0	0	0
Γ_5^-	2	-2	0	0	0	-2	2	0	0	0

$$H_{[000]}^{13} = \begin{pmatrix} t_5 & 0 & t_8 \\ 0 & t_6 & 0 \\ t_8 & 0 & t_7 \end{pmatrix} \quad (52)$$

$$H_{[000]}^{14} = \begin{pmatrix} t_9 & 0 & 0 \\ 0 & t_{10} & -t_{12} \\ 0 & -t_{12} & t_{11} \end{pmatrix}. \quad (53)$$

Then the rest of the hopping terms for cell $R = [000]$ can be derived by applying symmetry operations on sub-blocks one by one.

$$\begin{aligned} H_{[000]}^{21} &= H_{[000]}^{12\dagger} \\ H_{[000]}^{22} &= D(\sigma_z)H_{[000]}^{11}D^{-1}(\sigma_z) \\ H_{[000]}^{23} &= D(C_{2y})H_{[000]}^{11}D^{-1}(C_{2y}) \\ H_{[000]}^{31} &= H_{[000]}^{13\dagger} \\ H_{[000]}^{32} &= [D(C_{2y})H_{[000]}^{11}D^{-1}(C_{2y})]^\dagger \\ H_{[000]}^{33} &= D(i)H_{[000]}^{11}D^{-1}(i) \\ H_{[000]}^{34} &= D(C_{2x})H_{[000]}^{12}D^{-1}(C_{2x}) \\ H_{[000]}^{41} &= H_{[000]}^{14\dagger} \\ H_{[000]}^{43} &= H_{[000]}^{34\dagger} \\ H_{[000]}^{44} &= D(C_{2z})H_{[000]}^{11}D^{-1}(C_{2z}). \end{aligned}$$

Table 15. Double little group character table at M point in FBZ of Bi (110) $u = (\frac{1}{2}, \frac{1}{2}, 0)$.

M	E	$\{C_{2y} u\}$	$\{C_{2z} u\}$	C_{2x}	I	$\{\sigma_y u\}$	$\{\sigma_z u\}$	σ_x	\bar{E}	$\{\bar{C}_{2y} u\}$	$\{\bar{C}_{2z} u\}$	\bar{C}_{2x}	\bar{I}	$\{\bar{\sigma}_y u\}$	$\{\bar{\sigma}_z u\}$	$\bar{\sigma}_x$
M_1^+	2	0	0	0	2	0	0	0	2	0	0	0	2	0	0	0
M_1^-	2	0	0	0	-2	0	0	0	2	0	0	0	-2	0	0	0
M_2^+	1	1	-i	-i	1	1	-i	-i	-1	-1	i	i	-1	-1	i	i
M_3^+	1	-1	i	-i	1	-1	i	-i	-1	1	-i	i	-1	1	-i	i
M_4^+	1	1	i	i	1	1	i	i	-1	-1	-i	-i	-1	-1	-i	-i
M_5^+	1	-1	-i	i	1	-1	-i	i	-1	1	i	-i	-1	1	i	-i
M_2^-	1	1	-i	-i	-1	-1	i	i	-1	-1	i	i	1	1	-i	-i
M_3^-	1	-1	i	-i	-1	1	-i	i	-1	1	-i	i	1	-1	i	-i
M_4^-	1	1	i	i	-1	-1	-i	-i	-1	-1	-i	-i	1	1	i	i
M_5^-	1	-1	-i	i	-1	1	i	-i	-1	1	i	-i	1	-1	-i	i

Table 16. Double little group character table at X point in FBZ of Bi (110) $u = (\frac{1}{2}, \frac{1}{2}, 0)$.

X	E	$\{C_{2y} u\}$	$\{C_{2z} u\}$	C_{2x}	I	$\{\sigma_y u\}$	$\{\sigma_z u\}$	σ_x	\bar{E}	$\{\bar{C}_{2y} u\}$	$\{\bar{C}_{2z} u\}$	\bar{C}_{2x}	\bar{I}	$\{\bar{\sigma}_y u\}$	$\{\bar{\sigma}_z u\}$	$\bar{\sigma}_x$
X_1	2	0	0	2	0	0	0	0	2	0	0	0	2	0	0	0
X_2	2	0	0	-2	0	0	0	0	2	0	0	0	-2	0	0	0
X_3	2	0	0	0	0	0	0	-2i	-2	0	0	0	0	0	0	2i
X_4	2	0	0	0	0	0	0	2i	-2	0	0	0	0	0	0	-2i

For hopping terms from lattice sites in the home cell to surrounding cells, we start by considering hopping to cell $R = [100]$. The only two independent sub-blocks are $H_{[100]}^{11}$ and $H_{[100]}^{24}$:

$$H_{[100]}^{11} = \begin{pmatrix} 0 & 0 & 0 \\ 0 & 0 & t_{21} \\ 0 & -t_{21} & t_{20} \end{pmatrix} \quad (54)$$

$$H_{[100]}^{24} = \begin{pmatrix} 0 & 0 & 0 \\ 0 & t_{22} & 0 \\ 0 & 0 & t_{23} \end{pmatrix} \quad (55)$$

$$H_{[100]}^{21} = D(\sigma_x) H_{[000]}^{12\dagger} D^{-1}(\sigma_x)$$

$$H_{[100]}^{22} = D(\sigma_z) H_{[100]}^{11} D^{-1}(\sigma_z)$$

$$H_{[100]}^{23} = D(\sigma_x) H_{[000]}^{23} D^{-1}(\sigma_x)$$

$$H_{[100]}^{33} = D(C_{2x}) H_{[100]}^{11} D^{-1}(C_{2x})$$

$$H_{[100]}^{41} = D(\sigma_y) H_{[000]}^{14} D^{-1}(\sigma_y)$$

$$H_{[100]}^{42} = D(C_{2x}) H_{[100]}^{24} D^{-1}(C_{2x})$$

$$H_{[100]}^{43} = D(i) H_{[000]}^{21} D^{-1}(i)$$

$$H_{[100]}^{44} = D(\sigma_y) H_{[100]}^{11} D^{-1}(\sigma_y).$$

For hopping to cell $R = [010]$, the two independent sub-blocks are:

$$H_{[010]}^{11} = \begin{pmatrix} 0 & 0 & 0 \\ 0 & 0 & 0 \\ 0 & 0 & t_{24} \end{pmatrix} \quad (56)$$

$$H_{[010]}^{14} = \begin{pmatrix} t_{25} & t_{28} & t_{29} \\ -t_{28} & t_{26} & t_{30} \\ -t_{29} & t_{30} & t_{27} \end{pmatrix} \quad (57)$$

$$H_{[010]}^{21} = D(C_{2y}) H_{[000]}^{12} D^{-1}(C_{2y})$$

$$H_{[010]}^{22} = D(C_{2y}) H_{[010]}^{11} D^{-1}(C_{2y})$$

Table 17. Double little group character table at Y point in FBZ of Bi (110) $u = (\frac{1}{2}, \frac{1}{2}, 0)$.

Y	E	$\{C_{2y} u\}$	$\{C_{2z} u\}$	C_{2x}	I	$\{\sigma_y u\}$	$\{\sigma_z u\}$	σ_x	\bar{E}	$\{\bar{C}_{2y} u\}$	$\{\bar{C}_{2z} u\}$	\bar{C}_{2x}	\bar{I}	$\{\bar{\sigma}_y u\}$	$\{\bar{\sigma}_z u\}$	$\bar{\sigma}_x$
Y_1	2	0	0	0	0	0	0	2	2	0	0	0	0	0	0	2
Y_2	2	0	0	0	0	0	0	-2	2	0	0	0	0	0	0	-2
Y_3	2	0	0	-2i	0	0	0	0	-2	0	0	2i	0	0	0	0
Y_4	2	0	0	2i	0	0	0	0	-2	0	0	-2i	0	0	0	0

$$H_{[010]}^{23} = D(C_{2y})H_{[010]}^{14}D^{-1}(C_{2y})$$

$$H_{[010]}^{24} = D(C_{2y})H_{[000]}^{13}D^{-1}(C_{2y})$$

$$H_{[010]}^{33} = D(i)H_{[010]}^{11\dagger}D^{-1}(i)$$

$$H_{[010]}^{34} = D(C_{2z})H_{[000]}^{21}D^{-1}(C_{2z})$$

$$H_{[010]}^{44} = D(\sigma_z)H_{[010]}^{33}D^{-1}(\sigma_z).$$

For hopping to cell $R = [110]$, the only independent sub-block is:

$$H_{[110]}^{11} = \begin{pmatrix} t_{31} & t_{34} & t_{35} \\ -t_{34} & t_{32} & -t_{23} \\ t_{35} & t_{23} & t_{33} \end{pmatrix} \quad (58)$$

$$H_{[110]}^{21} = D(\sigma_z)H_{[000]}^{12}D^{-1}(\sigma_z)$$

$$H_{[110]}^{22} = D(\sigma_z)H_{[110]}^{11}D^{-1}(\sigma_z)$$

$$H_{[110]}^{23} = D(\sigma_x)H_{[010]}^{23}D^{-1}(\sigma_x)$$

$$H_{[110]}^{31} = D(\sigma_y)H_{[100]}^{24}D^{-1}(\sigma_y)$$

$$H_{[110]}^{33} = D(i)H_{[110]}^{11\dagger}D^{-1}(i)$$

$$H_{[110]}^{44} = D(\sigma_z)H_{[110]}^{33}D^{-1}(\sigma_z).$$

For hopping to cell $R = [1\bar{1}0]$, all the sub-blocks can be generated from the sub-blocks above:

$$H_{[1\bar{1}0]}^{11} = D(C_{2x})H_{[110]}^{33}D^{-1}(C_{2x})$$

$$H_{[1\bar{1}0]}^{13} = D(C_{2x})H_{[110]}^{31}D^{-1}(C_{2x})$$

$$H_{[1\bar{1}0]}^{22} = D(C_{2x})H_{[110]}^{44}D^{-1}(C_{2x})$$

$$H_{[1\bar{1}0]}^{33} = D(C_{2x})H_{[110]}^{11}D^{-1}(C_{2x})$$

$$H_{[1\bar{1}0]}^{41} = D(C_{2x})H_{[110]}^{23}D^{-1}(C_{2x})$$

$$H_{[1\bar{1}0]}^{43} = D(C_{2x})H_{[110]}^{21}D^{-1}(C_{2x})$$

$$H_{[1\bar{1}0]}^{44} = D(C_{2x})H_{[110]}^{22}D^{-1}(C_{2x}).$$

Lastly, for hopping to cell $R = [\bar{1}00]$, $R = [\bar{0}\bar{1}0]$, $R = [\bar{1}\bar{1}0]$ and $R = [\bar{1}10]$, they can be obtained by taking Hermit conjugate of the hopping listed above:

$$H_{[\bar{1}00]} = H_{[100]}^\dagger$$

$$H_{[0\bar{1}0]} = H_{[010]}^\dagger$$

$$H_{[\bar{1}\bar{1}0]} = H_{[110]}^\dagger$$

$$H_{[\bar{1}10]} = H_{[1\bar{1}0]}^\dagger.$$

Due to the non-trivial translation symmetry, the bands along the Brillouin zone boundaries are at least double degenerate. Similar to other allotropes, we calculate the basis functions of band representations near the Fermi level and list them in tables 9 and 10.

A.3. Character table for symmetry groups of three allotropes

The character tables for a Bi (111) bilayer and bismuthene can be derived from their corresponding point groups. Those character tables can be readily found in Koster's book [36]. Here we show the character table for a Bi (111) bilayer (D_{3d}) and bismuthene (D_{6h}) in tables 11 and 13, respectively. The character table for a Bi (110) bilayer involves nonsymmorphic symmetries and the characters for Γ , M , X and Y point are listed in tables 14 to 17.

ORCID iDs

- Qile Li  <https://orcid.org/0000-0001-7374-1692>
Jackson S Smith  <https://orcid.org/0000-0002-7769-7438>
Yuefeng Yin  <https://orcid.org/0000-0002-2958-1887>
Chutian Wang  <https://orcid.org/0000-0003-4701-3629>
Mykhailo V Klymenko  <https://orcid.org/0000-0002-4641-8977>
Jared H Cole  <https://orcid.org/0000-0002-8943-6518>
Nikhil V Medhekar  <https://orcid.org/0000-0003-3124-4430>

References

- [1] Hasan M Z and Kane C L 2010 *Rev. Mod. Phys.* **82** 3045
- [2] Bansil A, Lin H and Das T 2016 *Rev. Mod. Phys.* **88** 021004
- [3] Drozdov I K, Alexandradinata A, Jeon S, Nadji-Perge S, Ji H, Cava R J, Andrei Bernevig B and Yazdani A 2014 *Nat. Phys.* **10** 664
- [4] Liu Y and Allen R E 1995 *Phys. Rev. B* **52** 1566
- [5] Hsu C-H, Zhou X, Chang T-R, Ma Q, Gedik N, Bansil A, Xu S-Y, Lin H and Fu L 2019 *Proc. Natl Acad. Sci. USA* **116** 13255
- [6] König C, Greer J C and Fahy S 2021 arXiv:[2102.02018](https://arxiv.org/abs/2102.02018)
- [7] Liu Z, Liu C-X, Wu Y-S, Duan W-H, Liu F and Wu J 2011 *Phys. Rev. Lett.* **107** 136805
- [8] Murakami S 2006 *Phys. Rev. Lett.* **97** 236805
- [9] Munoz F, Vergniory M G, Rauch T, Henk J, Chulkov E V, Mertig I, Botti S, Marques M A L and Romero A H 2016 *Sci. Rep.* **6** 21790
- [10] Hsu C-H et al 2016 *Sci. Rep.* **6** 18993
- [11] Reis F, Li G, Dudy L, Bauernfeind M, Glass S, Hanke W, Thomale R, Schäfer J and Claessen R 2017 *Science* **357** 287
- [12] Schindler F et al 2018 *Nat. Phys.* **14** 918
- [13] Hirahara T, Bihlmayer G, Sakamoto Y, Yamada M, Miyazaki H, Kimura S-i, Blügel S and Hasegawa S 2011 *Phys. Rev. Lett.* **107** 166801
- [14] Wang Z F, Chen L and Liu F 2014 *Nano Lett.* **14** 2879
- [15] Ma Y, Dai Y, Kou L, Frauenheim T and Heine T 2015 *Nano Lett.* **15** 1083
- [16] Li S-s, Ji W-x, Li P, Hu S-j, Cai L, Zhang C-w and Yan S-s 2017 *ACS Appl. Mater. Interfaces* **9** 21515
- [17] Lu Y et al 2015 *Nano Lett.* **15** 80
- [18] Saito K, Sawahata H, Komine T and Aono T 2016 *Phys. Rev. B* **93** 041301
- [19] Nouri N, Rashedi G and Karbaschi H 2020 *Phys. Lett. A* **384** 126364
- [20] Bieniek M, Woźniak T and Potasz P 2017 *J. Phys.: Condens. Matter* **29** 155501
- [21] Mostofi A A, Yates J R, Lee Y-S, Souza I, Vanderbilt D and Marzari N 2008 *Comput. Phys. Commun.* **178** 685
- [22] Zak J 1989 *Phys. Rev. Lett.* **62** 2747
- [23] Klymenko M V, Vaitkus J A, Smith J S and Cole J H 2021 *Comput. Phys. Commun.* **259** 107676
- [24] Wada M, Murakami S, Freimuth F and Bihlmayer G 2011 *Phys. Rev. B* **83** 121310
- [25] Li X, Liu H, Jiang H, Wang F and Feng J 2014 *Phys. Rev. B* **90** 165412
- [26] Remediakis I N and Kaxiras E 1999 *Phys. Rev. B* **59** 5536
- [27] Yang F et al 2012 *Phys. Rev. Lett.* **109** 016801
- [28] Kresse G and Furthmüller J 1996 *Phys. Rev. B* **54** 11169
- [29] Kresse G and Furthmüller J 1996 *Comput. Mater. Sci.* **6** 15
- [30] Perdew J P, Burke K and Ernzerhof M 1996 *Phys. Rev. Lett.* **77** 3865
- [31] Mostofi A A, Yates J R, Pizzi G, Lee Y-S, Souza I, Vanderbilt D and Marzari N 2014 *Comput. Phys. Commun.* **185** 2309
- [32] Marzari N, Mostofi A A, Yates J R, Souza I and Vanderbilt D 2012 *Rev. Mod. Phys.* **84** 1419
- [33] Gresch D, Wu Q, Winkler G W, Häuselmann R, Troyer M and Soluyanov A A 2018 *Phys. Rev. Materials* **2** 103805
- [34] Huang Z-Q, Chuang F-C, Hsu C-H, Liu Y-T, Chang H-R, Lin H and Bansil A 2013 *Phys. Rev. B* **88** 165301
- [35] Kochan D, Irmer S and Fabian J 2017 *Phys. Rev. B* **95** 165415
- [36] Koster G F 1963 *Properties of the Thirty-Two Point Groups* (Cambridge, MA: MIT Press)
- [37] Fu L and Kane C L 2007 *Phys. Rev. B* **76** 045302
- [38] Yakovkin I N 2019 *J. Phys. Chem. Solids* **129** 277
- [39] Du H et al 2016 *Nat. Commun.* **7** 1
- [40] Nagao T et al 2004 *Phys. Rev. Lett.* **93** 105501

- [41] Miao L *et al* 2015 *Phys. Rev. B* **91** 205414
- [42] Zhang K F, Yang F, Song Y R, Liu C, Qian D, Gao C L and Jia J-F 2015 *Appl. Phys. Lett.* **107** 121601
- [43] Kowalczyk P J *et al* 2020 *ACS Nano* **14** 1888
- [44] Zhu S-Y *et al* 2019 *Nano Lett.* **19** 6323
- [45] Zhang J-J, Zhang Y and Dong S 2018 *Phys. Rev. Materials* **2** 126004
- [46] Kou L, Ma Y, Sun Z, Heine T and Chen C 2017 *J. Phys. Chem. Lett.* **8** 1905
- [47] Acosta C M and Fazzio A 2019 *Phys. Rev. Lett.* **122** 036401
- [48] Su W P, Schrieffer J R and Heeger A J 1979 *Phys. Rev. Lett.* **42** 1698
- [49] Gröning O *et al* 2018 *Nature* **560** 209
- [50] Dresselhaus M S, Dresselhaus G and Jorio A 2008 *Group Theory: Application to the Physics of Condensed Matter* 1st edn (Berlin: Springer)